Effect of three-dimensionality on the lift and drag of nominally two-dimensional cylinders

R. Mittal and S. Balachandar
Department of Theoretical and Applied Mechanics, 104 S. Wright St., 216 Talbot Lab, University of Illinois at Urbana–Champaign, Urbana, Illinois 61801

(Received 12 December 1994; accepted 11 April 1995)

It has been known for some time that two-dimensional numerical simulations of flow over nominally two-dimensional bluff bodies at Reynolds numbers for which the flow is intrinsically three dimensional, lead to inaccurate prediction of the lift and drag forces. In particular, for flow past a normal flat plate (*International Symposium on Nonsteady Fluid Dynamics*, edited by J. A. Miller and D. P. Telionis, 1990, pp. 455–464) and circular cylinders [J. Wind Eng. Indus. Aerodyn. **35**, 275 (1990)], it has been noted that the drag coefficient computed from two-dimensional simulations is significantly higher than what is obtained from experiments. Furthermore, it has been found that three-dimensional simulations of flows lead to accurate prediction of drag [J. Wind Eng. Indus. Aerodyn. **35**, 275 (1990)]. The underlying cause for this discrepancy is that the surface pressure distribution obtained from two-dimensional simulations does not match up with that obtained from experiments and three-dimensional simulations and a number of reasons have been put forward to explain this discrepancy. However, the details of the physical mechanisms that ultimately lead to the inaccurate prediction of surface pressure and consequently the lift and drag, are still not clear. In the present study, results of two-dimensional and three-dimensional simulations of flow past elliptic and circular cylinders have been systematically compared in an effort to pinpoint the exact cause for the inaccurate prediction of the lift and drag by two-dimensional simulations. The overprediction of mean drag force in two-dimensional simulations is directly traced to higher Reynolds stresses in the wake. It is also found that the discrepancy in the drag between two-dimensional and three-dimensional simulations is more pronounced for bluffer cylinders. Finally, the current study also provides a detailed view of how the fluctuation, which are associated with the Kármán vortex shedding in the wake, affect the mean pressure distribution and the aerodynamic forces on the body.

I. INTRODUCTION

Starting from a steady wake, the flow over bluff bodies undergoes a sequence of transitions as the Reynolds number is increased. For example, in the case of a circular cylinder the wake transitions from a steady to an unsteady state at a Reynolds number, Re, (based on the diameter, $\mathfrak{D}$) of about 49 and the well-known Kármán vortex street is observed. The second bifurcation occurs at around Re=180, at which there is a transition from a two-dimensional to a three-dimensional wake. According to Williamson,[1] the three-dimensionality at these low Reynolds numbers manifests itself in the form of vortex loops and pairs of streamwise vortices, which have a characteristic spanwise wavelength of about $3\mathfrak{D}$. Next in the Reynolds number range of 230–260, a gradual transition occurs where the vortex loops give way to fine-scale streamwise vortices with a spanwise spacing of about $\mathfrak{D}$. A further transition occurs at around $\mathrm{Re}=10^5$, the so-called critical Reynolds number, where the boundary layer becomes turbulent before separation.

The variation of base suction pressure (BSP) coefficient (suction pressure on the wake side of the cylinder) for a circular cylinder, as given by Williamson and Roshko[2] and Williamson[3] is shown in Fig. 1. The drag over the cylinder is directly related to the base suction pressure, and thus insight into the variation of drag with Reynolds number can be gained by studying the corresponding variation in BSP. It can be seen from this plot that BSP undergoes sharp variations at all of the above-mentioned transition points, and a thorough account of the flow behavior after each of these transitions has been given by Roshko.[4] In the steady regime (Re<49), the decrease in BSP with increasing Re is due to the increase in size of the steady recirculation bubble. In the unsteady regime (49<Re<180) the increase in BSP is due to the increase in stresses in the near-wake region[2] and the shrinking of the vortex formation region. At Re=180, there is a drop in BSP that is thought to be associated with a decrease in the stresses in the near-wake due to three-dimensionality. The BSP rises further until about Re=260, where it exhibits a sharp local maximum, and it has been conjectured that this is due to the saturation of the primary instability growth.[4] With increasing Re, there is increasing disorder in the three-dimensional structures leading to a further decrease in the stresses and a corresponding decrease in BSP. When the Reynolds number is increased beyond 1500, there appears an instability in the separating shear layer, which leads to an increase in the stresses and BSP. The BSP continues to increase until the critical Reynolds number at which there is a steep drop in BSP associated with turbulent separation and reduction in the width of the wake.

Thus, above a Reynolds number of 180, three-dimensionality plays a significant role in determining the structure of the wake and a two-dimensional (2-D) simulation of such a flow would fail to capture the effect of three-dimensional

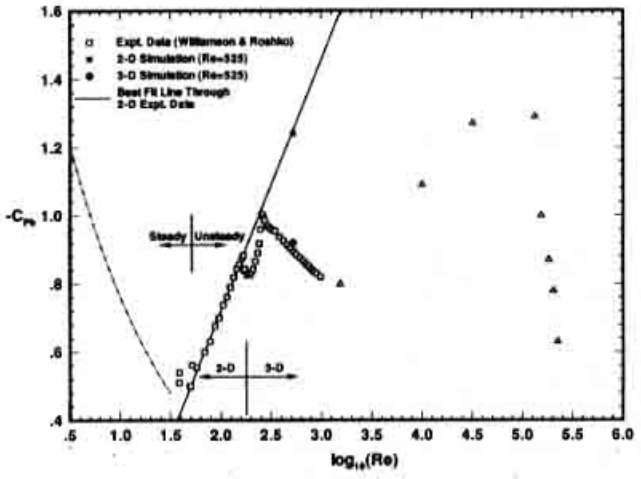

FIG. 1. Plot of base suction pressure for flow past a circular cylinder compiled from data from Refs. 2, 26, and 27. The solid line extends the behavior of the 2-D unsteady base pressure coefficient past Re=180. Results from the current 2-D and 3-D simulation of Case II have also been plotted.

structures on the flow field. In fact, 2-D simulations are known to overpredict the drag coefficient for Reynolds numbers beyond which the actual flow is observed to be three dimensional.[5,6] On the other hand, corresponding 3-D simulations predict the drag coefficient accurately.[6] The present simulations show that in addition to the drag, there are also differences in the lift variation obtained from 2-D and 3-D simulations, and both the mean as well as the peak-to-valley fluctuation levels of these global quantities are smaller in the 3-D simulations. Furthermore, it is found that these effects of three-dimensionality on lift and drag depend on geometry effects such as thickness ratio and angle of attack.

The details of the mechanisms that are responsible for the decrease in BSP resulting from the two-dimensional to three-dimensional flow transition observed in experiments (at Re=180), are not completely understood. Similar mechanisms are believed to be responsible for the differences in the drag coefficient obtained from 2-D and 3-D simulations. Over the years, several possible explanations have been put forth as follows.

(i) One possible reason for the difference could be the end effects from the termination of the body at the walls of the wind tunnel or at the endplates.[5] Also, in experiments it has been observed that end effects can lead to oblique shedding,[7,8] a situation where the shedding is out of phase in the spanwise direction, and this could possibly result in the discrepancy between 2-D and 3-D simulations.

(ii) It has also been suggested by Chua *et al.*[5] that even in the absence of nonparallel shedding, imperfect spanwise pressure correlation could result from small-scale three-dimensional effects, and this could directly lead to a drop in the peak-to-valley level of the lift and drag coefficients. If the shedding is out of phase in the spanwise direction, the sectional forces will peak at different times, thereby reducing the peak values of the integrated forces.

(iii) It has been argued previously that in the wake bubble, the pressure and shear stresses are roughly in equilibrium,[9] therefore, differences in the shear stresses imply differences in the wake pressure distribution. In experiments and 3-D simulations, the presence of spanwise fluctuations and the streamwise component of vorticity leads to substantial differences in the Reynolds and total stress components in the wake. This, in turn, affects the pressure distribution and hence the drag on the body. In support of this hypothesis, Williamson and Roshko[2] report a reduction in the measured "in-plane" shear stress with increasing three-dimensionality and an accompanying decrease in base suction over a Reynolds number range of 260–1500.

(iv) Another relevant observation made by Chua *et al.*[5] in their 2-D simulations over a normal flat plate is that the computed vortices form much closer to the plate than in the experiments. This has been put forward as a possible cause for higher suction in the two-dimensional flow. A shorter vortex formation length is thought to be caused by the higher Reynolds stresses in 2-D simulations.

(v) Tamura *et al.*[6] have performed simultaneous 2-D and 3-D simulations of flow past circular cylinders for Reynolds number varying from 20 to 10^6 and they conclude that the presence of secondary vortices in 2-D simulations has a "strong influence" on the aerodynamics and leads to higher suction in the wake. They also claim that these secondary vortices are absent in 3-D simulations, since spanwise velocities are allowed. Furthermore, they observe that the 3-D simulations (for $Re=10^3-10^6$) predict the drag coefficients and the drag crisis very well in contrast to the 2-D simulations.

Thus, the above clearly point to a need for further investigation into this issue in order to precisely elucidate the physical mechanisms that are responsible for a lack of agreement between the results of 2-D and 3-D simulations. An accurate prediction of lift and drag is of paramount importance, since these two are often the most sought after quantities by aero- and hydrodynamacists. Three-dimensional simulations of flow over complex bodies have become possible only in the recent years, but remain very expensive and are thus limited to moderate Reynolds numbers. On the other hand, 2-D simulations are quite feasible, even for complex geometries and relatively high Reynolds numbers. Thus, it is not uncommon to use 2-D simulations to predict the aerodynamic characteristics of a wing or the wind loads on a skyscraper, etc. It would therefore be useful to know the limitations of 2-D simulations in predicting gross aerodynamic quantities. Furthermore, an understanding of the basic mechanisms that result in the discrepancy between two-dimensional and three-dimensional results could eventually lead to the incorporation of additional physics, which would allow 2-D simulations to predict the aerodynamic forces more accurately.

In the present study, we investigate in detail the effect of three-dimensionality on lift and drag. Flow is studied for the three configurations that are shown in Fig. 2. A direct numerical simulation methodology has been developed in Ref. 10 to solve the flow over elliptic and circular cylinders, which allows us to study the effects of the angle of attack as well as the thickness ratio. In Fig. 2, $Re^*=U_\infty L^*/\nu$, where L^* is the projected width of the cylinder, U_∞ is the free-stream velocity, and ν is the kinematic viscosity of the

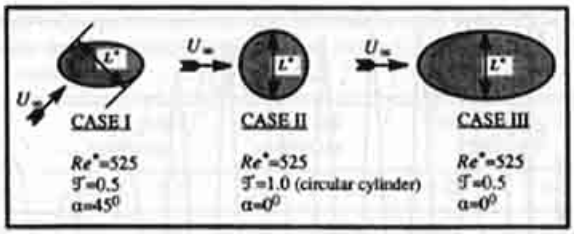

FIG. 2. Geometry and parameters for the three cases that have been studied.

fluid. Furthermore, $\mathscr{T}$ is the thickness ratio of the ellipse that is equal to L_Y/L_X, where L_Y and L_X are the semiminor and semimajor axes of the elliptic cylinder, respectively. Finally, α is the angle of attack of the cylinder. The schematic in Fig. 3 describes the coordinate system.

For the configurations shown in Fig. 2, 2-D as well as 3-D simulations are carried out and a detailed comparison is made of the flow obtained from the two simulations. It is found that even in the absence of end effects and oblique shedding, there is a substantial difference in the forces computed from 2-D and 3-D simulations. Time-averaged quantities are computed and used to identify those features of the flow that are instrumental in producing the difference between the aerodynamic forces computed from 2-D and 3-D simulations. The effect of the Reynolds stresses on the pressure distribution is computed, and it is concluded that the differences in the in-plane (x-y plane) Reynolds stresses are the primary cause for the drop in the average level of drag in 3-D simulations. Furthermore, it is also found that at the same effective Reynolds number, the differences between the 2-D and 3-D simulations, are more significant for bluffer cylinders. Large differences are found in the peak-to-valley amplitude level of lift obtained from 2-D and 3-D simulations for all the three cases, and the underlying cause for this is also investigated. Also, in addition to studying the mechanisms that lead to the discrepancy between 2-D and 3-D simulations, insight into the role of unsteadiness in determining the pressure in the wake and on the body is also provided, and this we hope, will assist in the development of better wake models.

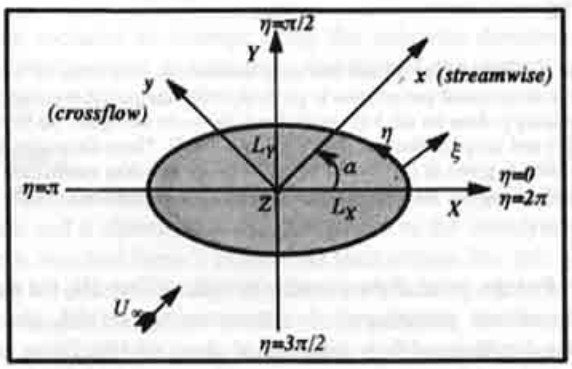

FIG. 3. Schematic showing the coordinate system that has been employed.

II. SIMULATION METHODOLOGY

The governing equations for the flow are the full three-dimensional, incompressible Navier–Stokes equations, and a Fourier–Chebyshev spectral collocation methodology is used to simulate the flow in a body fitted elliptic cylindrical grid. The azimuthal direction (η) is intrinsically periodic and a Fourier expansion is used in that direction. Also, the flow is considered to be periodic along the spanwise direction with period L_Z, and therefore a Fourier expansion is also employed along Z. Here spanwise periodicity is used as a model for flow over a cylinder with an infinite spanwise extent. Flow visualization studies have shown that for Reynolds numbers in the range $180<\mathrm{Re}<1000$, the circular cylinder wake is dominated by structures that have a well-defined periodic structure in the spanwise direction.[3,11] Furthermore, similar streamwise structures have also been observed in plane wakes,[12] in the wake of a normal flat plate[13] and in wakes of elliptic cylinders,[14,15] indicating a similarity in the topological structure of all wakes. Thus, imposition of periodicity in the spanwise direction coupled with an appropriately chosen spanwise length should ensure faithful reproduction of the important physics of the flow field for all the cylinders chosen in the present study. The spanwise length L_Z for the present simulations is chosen to be equal to $2L_X$, which should allow us to capture at least one pair of streamwise structures for all the cylinders studied in the present investigation. Visualization of vortical structures shows that in the present simulation, there are two pairs of counter-rotating streamwise vortices in the circular cylinder wake.[14,15] Furthermore, for the elliptic cylinder at 45° and 0° angle of attack, one and three pairs of streamwise vortical structures are observed, respectively.[16]

The wall–normal direction (ξ) is nonperiodic, and therefore a Chebyshev expansion is used for discretization. The infinite flow domain is truncated to a finite but large computational domain and nonreflecting boundary conditions are applied at the outflow boundary. Furthermore, a new mixed boundary condition is applied at the inflow boundary, which allows the incoming flow to adjust to the displacement effect of the body. A two-step, time-split method is employed to advance the solution in time through the advection-diffusion and pressure-correction steps. A homogeneous Neumann pressure boundary condition is used on the body in conjunction with a higher-order intermediate velocity boundary condition. These boundary conditions satisfy no-penetration exactly and no-slip to $O(\Delta t^3)$ accuracy on the cylinder surface, where Δt is the time-step size.

Details of the numerical method are given in Mittal and Balachandar,[10,16] where it has also been demonstrated that the outflow boundary condition is capable of convecting large disturbances out of the computational domain without spurious reflections. Quantities like lift, drag, and Strouhal number of vortex shedding are also shown to be independent of the size of the computational domain, thus establishing that the boundary conditions at the outer boundary have no effect on the flow dynamics. Furthermore, it has also been shown that the intermediate velocity and pressure boundary conditions on the body, which are used in conjunction with two-step time-split method, accurately predict all flow quan-

tities on the body, including pressure and vorticity.

For all of the simulations, the initial condition is assumed to be the corresponding potential flow, and the two-dimensional viscous flow is subsequently obtained by imposing no-slip boundary conditions on the body. At nonzero angles of attack, the shedding process is initiated naturally by the asymmetry of the geometry, but at a zero angle of attack, shedding is initiated deliberately by providing a small "conveyor-belt"-type of slip velocity on the body, which varies sinusoidally for a short period of time.[10] This perturbation has the desirable property that it neither produces any divergence nor any net circulation. Once the shedding process is well established and all the initial transients have exited the computational domain, three-dimensionality is initiated by allowing a small slip velocity on the body for a short duration, which is random in the spanwise direction as well as in time. Thereafter, the three-dimensional flow is allowed to develop and saturate on its own.

III. RESULTS AND DISCUSSION

In this section, results obtained for the three cases shown in Fig. 2 will be presented. For Case I, the 2-D and 3-D simulations have been performed on 81×100 ($\xi\times\eta$) and a $81\times100\times28$ ($\xi\times\eta\times z$) grid, respectively. For the other two cases, computations have been performed on a 81×160 ($\xi\times\eta$) grid for 2-D simulations and on a $81\times160\times40$ ($\xi\times\eta\times z$) grid for 3-D simulations. In all of the simulations, the outer boundary is placed at $30L_X$ from the body and the nondimensional time step size (Δt) is 1.5×10^{-3}.

A. Comparison of 2-D and 3-D simulation results

Figures (4a), (4b), and (4c) show the variation of lift and drag coefficients with time for Cases I, II and III, respectively. The coefficients of lift and drag are defined as $C_L=L/\frac{1}{2}\rho U_\infty^2 2L_Y L_Z$ $C_D=D/\frac{1}{2}\rho U_\infty^2 2L_Y L_Z$, respectively, for 3-D simulations, where L and D are the spanwise integrated lift and drag forces, respectively, and ρ is the density of the fluid. Corresponding definitions for 2-D simulations do not have the spanwise length in the denominator. In all of these figures, we show the variation of the lift and drag coefficients as the flow transitions from a saturated two-dimensional to a fully three-dimensional flow. Table I lists the mean and peak-to-valley amplitude levels of the force coefficients obtained for each of these cases from the 2-D and 3-D simulations. The mean and peak-to-valley values have been obtained for one representative shedding cycle in the 2-D and 3-D simulations.

For Case I, the three-dimensional perturbation is introduced at $t=68$, and over the next 30 time units, the three-dimensionality grows to sufficient amplitude so as to alter the lift and drag on the body. Beyond $t=90$, a drastic reduction in the average as well as the peak-to-valley level of lift and drag can be observed. From Table I we note that the the mean lift and drag levels computed from 2-D simulations are larger than those computed from 3-D simulation by about 11% and 39%, respectively. Furthermore, the peak-to-valley level of lift is also about 261% larger in the 2-D simulation than for the corresponding 3-D simulation.

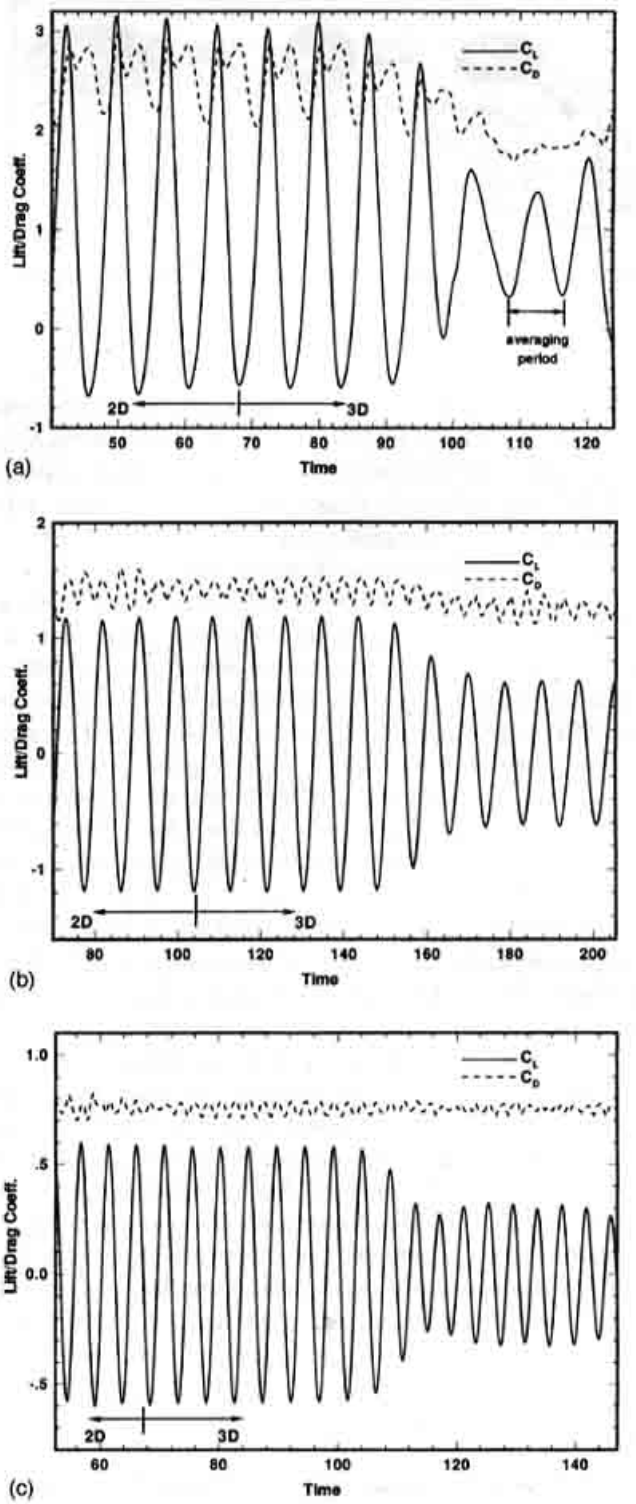

FIG. 4. (a) Variation of lift and drag coefficients with time for Case I. Three-dimensional perturbation is given at $t=68$. The period over which the averaging is done for the 3-D simulation is shown in the figure. (b) Variation of lift and drag coefficients with time for Case II. Three-dimensional perturbation is given at $t=105$. (c) Variation of lift and drag coefficients with time for Case III. Three-dimensional perturbation is given at $t=67.5$.

For the case of the circular cylinder (Case II), the three-dimensional perturbation is introduced at $t=105$, and the three-dimensional flow saturates at about $t=180$. From Table I it is noted that the mean drag coefficient is 1.24 for the 3-D simulations. Experiments on circular cylinders estimate the

TABLE I. Comparison between mean and peak-to-valley levels of the aerodynamic force coefficients obtained from 2-D and 3-D simulations of the three cases.

Case No.	Mean drag coefficient		Mean lift coefficient		Peak-to-valley lift coefficient	
	2-D	3-D	2-D	3-D	2-D	3-D
I	2.52	1.81	0.97	0.86	3.91	1.08
II	1.44	1.24	0.00	0.00	2.42	1.28
III	0.78	0.77	0.00	0.00	1.21	0.62

drag coefficients at this Reynolds number to be in the range 1.15–1.2,[17,18] therefore the 3-D simulation predicts the drag more accurately than the 2-D simulation, which predicts a 16% larger drag. Furthermore, the peak-to-valley level of lift in the 2-D simulation is about 88% larger than for the corresponding 3-D simulations.

For Case III, the three-dimensional perturbation is introduced at $t=67.5$ and the three-dimensionality saturates at around $t=115$. From Table I we note that there is only a small (~1%) difference in the average level of drag, however, there is a significant (~94%) overestimation of the peak-to-valley level of lift in the 2-D simulation.

Thus, it is observed that the geometry of the cylinder as seen by the incoming flow, has a very noticeable effect on the overall discrepancy in the aerodynamic forces obtained from 2-D and 3-D simulations. In particular, it is noted that the discrepancy in the mean drag level is larger for bluffer bodies. However, the peak-to-valley level of lift is grossly overpredicted by 2-D simulations for all the three configurations.

In order to obtain a better idea of the difference in the overall flow fields obtained from 2-D and 3-D simulations, the pressure and spanwise vorticity (ω_z) fields have been averaged over one shedding cycle, and the results are shown in the following figures. In the 2-D simulations, the average of a variable "f" is defined as

$$\bar{f}(\xi,\eta)=\frac{1}{T}\int_0^T f(\xi,\eta,t)dt, \tag{1}$$

where T is the time period of shedding. For 3-D simulations, the average is defined as

$$\bar{f}(\xi,\eta)=\frac{1}{T}\frac{1}{L_z}\int_0^{L_z}\int_0^T f(\xi,\eta,z,t)dt\,dz, \tag{2}$$

which includes an average along the spanwise direction as well. Furthermore, in both these simulations, the perturbation f' can be defined as $f'=f-\bar{f}$.

1. Case I

This case is of an elliptic cylinder at a large angle of attack and it shows dramatic differences in the aerodynamic forces obtained from 2-D and 3-D simulations. For this case it can be observed in Fig. 4(a) that the shedding cycle in the three-dimensional flow is not strictly periodic, and the time average is over the cycle indicated in the figure. Figures 5(a) and 5(b) show the average spanwise vorticity fields ($\bar{\omega}_z$) obtained from the 2-D and 3-D simulations, respectively. The one striking difference between the two fields is the location of the center of the rolled up vortices. In the 2-D flow, the counterclockwise vortex rolls up approximately 0.55 units away from the cylinder surface, whereas in the 3-D flow, this vortex rolls up at a distance of about 1.2 units. This is, in general, in agreement with Chua *et al.*,[5] who observe that the vortices computed from 2-D simulations roll up closer to the flat plate than what is observed in experiments.

Contours of the average pressure coefficient ($C_{\bar{P}}$) for the 2-D and 3-D simulations are shown in Figs. 6(a) and 6(b), respectively. It can observed that the center of low pressure in the wake for the 2-D simulation lies at a distance of about 0.54 units from the cylinder surface, whereas for the 3-D simulation it lies about 1.5 units away. The low-pressure region in the wake for the 2-D simulation is also found to be much more intense ($C_{\bar{P}_{\min}}=-2.08$) than for the 3-D simulation ($C_{\bar{P}_{\min}}=-1.26$). It will be shown in a later section that this low-pressure region is primarily due to Reynolds stresses in the wake region, and higher Reynolds stresses in the 2-D simulation are what lead to a lower pressure in the wake. We also observe that the center of low pressure in the 2-D simulation just like the rolled up vortices, has been drawn closer to the body than in the 3-D simulation, and this too is connected to a higher level of Reynolds stresses in the 2-D simulation acting close to the body.

The distributions of $C_{\bar{P}}$ and the mean skin-friction coefficient, $C_{\bar{F}}$, on the surface of the cylinder for the 2-D and 3-D simulations, have been plotted in Fig. 7. It is apparent from the distribution of $C_{\bar{F}}$ that the contribution of viscous shear stress toward lift and drag is small compared to that of pressure. In fact, shear stress contributes, at most, about 10% to the total drag for both the 2-D and 3-D simulations. Thus, for the purpose of investigating lift and drag, it is reasonable to limit the analysis to the pressure effect. There are, however, some interesting observations that can be made regarding the skin friction coefficient. First, $C_{\bar{F}}=0$ indicates the presence of stagnation or separation points, and allows us to identify the separation region. For this case, it can be seen that the wake lies roughly in the region $0<\eta<0.8\pi$. Second, the skin-friction coefficient is directly proportional to the surface spanwise vorticity and conclusions regarding vorticity production on the body can also be drawn from the skin friction coefficient.

It can be observed that in contrast to the 2-D simulation, the pressure shows little variation in the wake region for the 3-D simulation. Thus, uniformity in pressure seems to be a universal feature of three-dimensional bluff body wakes, since similar behavior has been observed in the wake of circular cylinders by Tamura *et al.*,[2] in the wake of normal flat plates by Fage and Johansen[19] and Najjar,[13] and in the other two cases to be reported here as well. Furthermore, the largest difference in the surface pressure distributions is found to be in the vicinity of the two separation points (located roughly at $\eta=0$ and 0.8π).

It can also be observed that there are noticeable differences in the surface pressure as well as the surface spanwise vorticity computed from 2-D and 3-D simulations even upstream of the separated wake region. In particular, the pressure at the front stagnation point (located roughly at

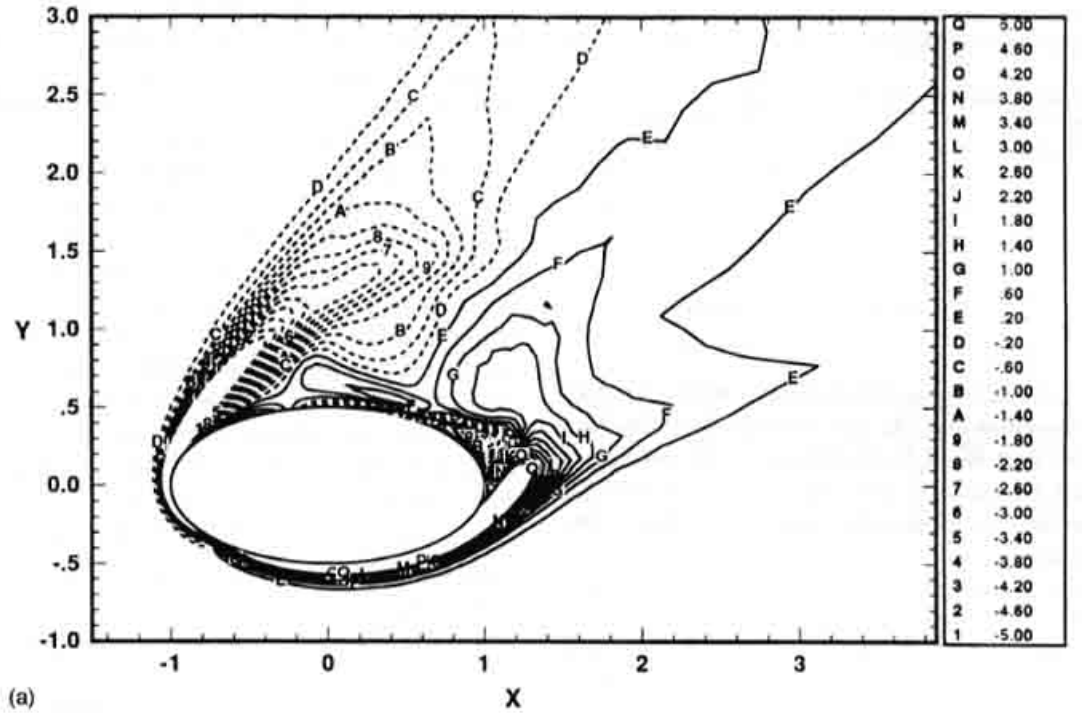

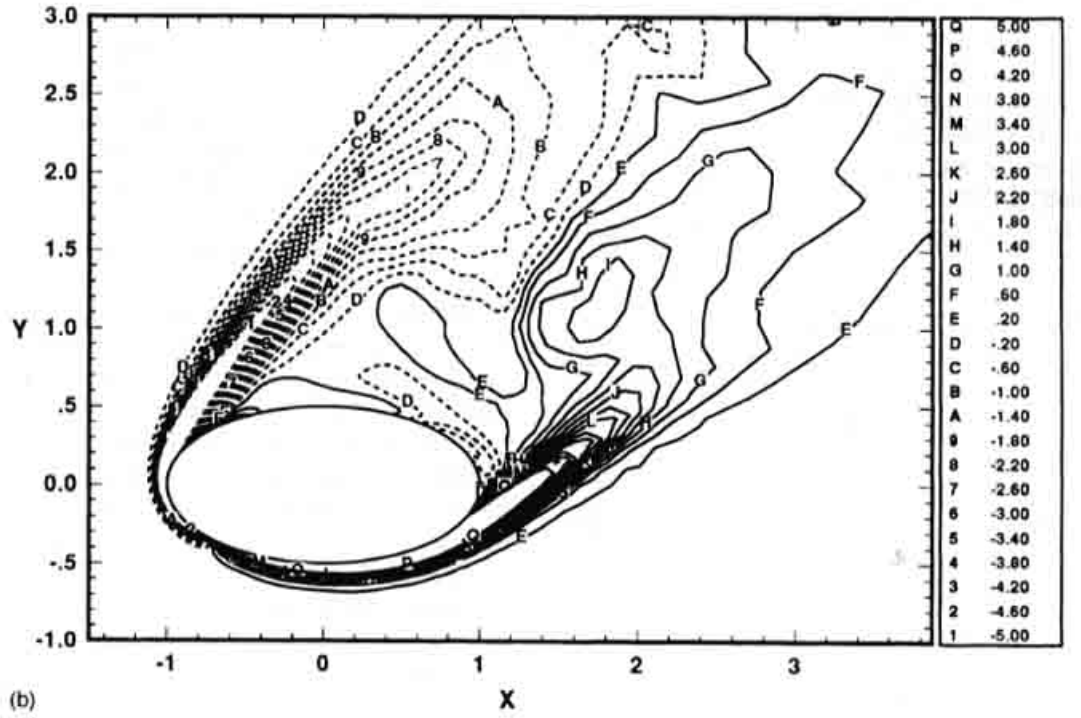

FIG. 5. (a) Contours of $\bar{\omega}_z$ for the 2-D simulation of Case I. Solid and dashed contour lines correspond to positive and negative values, respectively. (b) Contours of $\bar{\omega}_z$ for the 3-D simulation of Case I. Solid and dashed contour lines correspond to positive and negative values, respectively.

$\eta=1.25\pi$) is lower for the 3-D simulation. The surface spanwise vorticity too is slightly lower in magnitude everywhere for the 3-D simulation. This is at first puzzling, since even in the 3-D simulation, the unseparated boundary layer region upstream of the wake is nearly two dimensional and no significant differences are therefore expected in this upstream region between the 2-D and 3-D simulations. This reduction in the surface vorticity in the upstream attached portion of the boundary layer and associated decrease in the vorticity production leads to the formation of weaker shear layers and the delayed roll-up of the Kármán vortices in 3-D simulations.

This apparent discrepancy can be explained by considering a well-established two-dimensional flow, where three-dimensionality has just been "turned on" (i.e., the flow is given a small three-dimensional perturbation). Initially, the vorticity production and pressure distribution on the body are those corresponding to the two-dimensional flow. However,

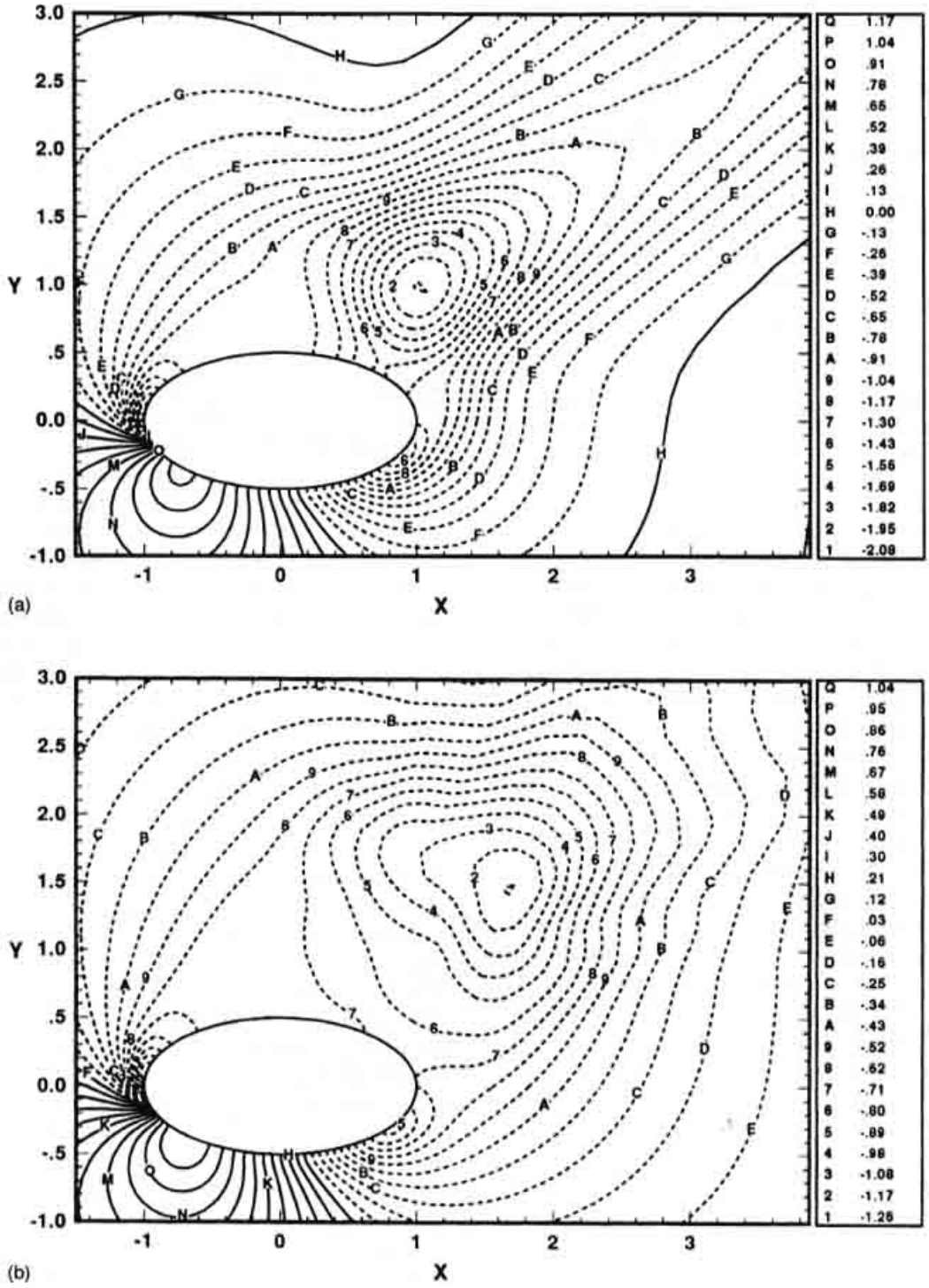

FIG. 6. (a) Contours of mean pressure coefficient, $C_{\bar{p}}$, for the 2-D simulation of Case I. Solid and dashed contour lines correspond to positive and negative values, respectively. (b) Contours of mean pressure coefficient, $C_{\bar{p}}$, for the 3-D simulation of Case I. Solid and dashed contour lines correspond to positive and negative values, respectively.

as time passes, the wake starts to establish three-dimensionality through stretching and bending of vortex filaments, and the vorticity distribution in the wake changes. It can be shown that the vorticity field uniquely determines the velocity field around the cylinder,[20] and therefore changes in the vorticity distribution in the wake affect the entire velocity field. The vorticity production at the body also adjusts to the changing velocity field, so as to satisfy no slip at the body, thus leading to a slightly different vorticity distribution, even in the unseparated region upstream of the wake. Consequently, the tangential pressure gradient, which is related to the tangential vorticity source strength[20] also gets altered, leading to a different pressure distribution in the unseparated boundary layer region. To sum up the above discussion we quote Lighthill:[20] "the vorticity which is produced at the surface, and carried away from it by diffusion and convec-

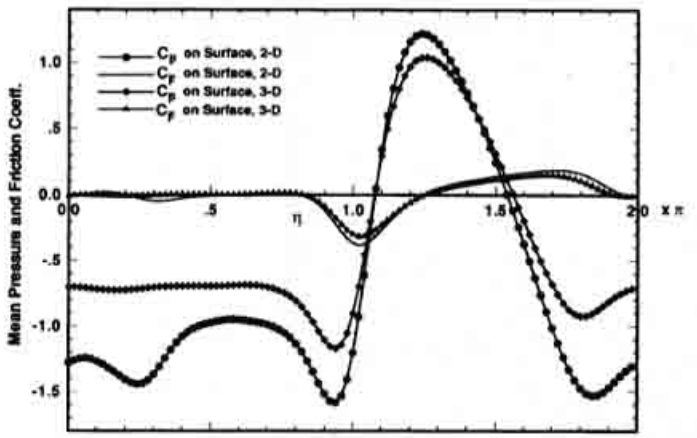

FIG. 7. Surface distribution of mean pressure, $C_{\bar{p}}$, and skin-friction coefficient, $C_{\bar{f}}$, for Case I. Results of both 2-D and 3-D simulations have been plotted for comparison.

tion, determines the entire flow, whose development in turn controls the production of vorticity."

It is clear that extrinsic three-dimensional phenomena resulting from end effects are ruled out as a possible cause of lift and drag reduction in the 3-D simulation, since these extrinsic three-dimensional mechanisms are absent here, owing to the assumption of periodicity in the spanwise direction. To investigate if imperfect spanwise correlation in the shedding process is responsible for the drop in the mean and peak-to-valley levels of lift and drag forces in 3-D simulations, we have plotted in Fig. 8 the spanwise variation of sectional lift and drag coefficients at five stages in the shedding cycle. It can be seen from the lift variation that the shedding is nearly two dimensional and is quite well correlated across the span, and the small spanwise variation cannot account for the larger reduction in the peak-to-valley level of lift. Therefore, the drop in the average and peak-to-valley levels of both lift and drag can only be attributed to other intrinsic three-dimensional effects.

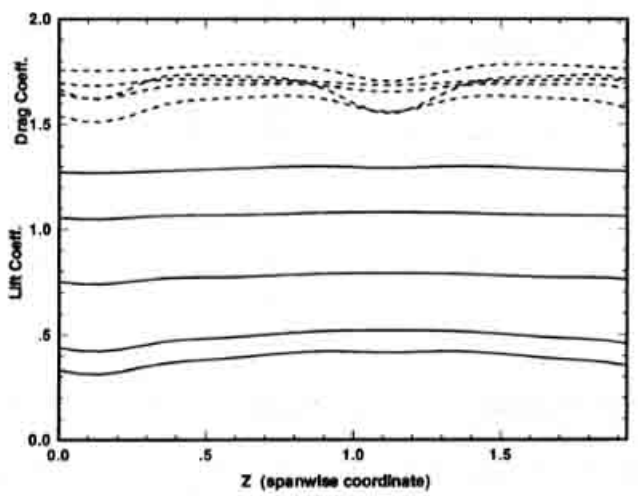

FIG. 8. Spanwise variation of sectional lift and drag coefficients during a shedding cycle for Case I. Solid lines correspond to lift coefficient and dashed to drag coefficient. Both show relatively small variations in the spanwise direction, indicating that the shedding is well correlated across the span.

2. Case II

The circular cylinder is a canonical geometry for bluff body wakes and there is a vast amount of experimental and numerical data for flow over circular cylinders. The Reynolds number range of 50–500 has been of particular interest in recent years, and a number of studies have investigated the wake structure and dynamics of the flow in this range.[2,3,8,21] Thus, comparisons of the current results of 2-D and 3-D simulations with the results from some of these studies will give us an idea about the relative fidelity of the simulations.

Figures 9(a) and 9(b) show mean spanwise vorticity contours for the 2-D and 3-D simulations, respectively. It can be observed that for the 3-D simulation, the vortices extend farther downstream than for the 2-D simulation. This is similar to the observations made for the previous case. Since the vortices in the 2-D simulation do not have a well-defined center, it is not straightforward to compare the strength of the vortices, however, the level of vorticity is found to be generally higher in the 2-D simulation. Figures 10(a) and 10(b) show the corresponding $C_{\bar{p}}$ distribution for the 2-D and 3-D simulations, respectively, and it can be observed that the center of the low-pressure region in the wake for the 2-D simulation is closer than for the 3-D simulation by about 0.4 units. It is also noted that the pressure at the center of the low-pressure region for the 2-D simulation is lower ($C_{\bar{p}_{\min}} = -1.84$) than for the 3-D simulation ($C_{\bar{p}_{\min}} = -1.46$).

Figure 11 shows the mean pressure coefficient on the cylinder surface for the 2-D and 3-D simulations. One can observe that there is a noticeable difference in the pressure in the wake, and this is the primary cause for the reduction in drag. Note that the base suction pressure coefficient (at $\eta=0$) obtained from the 3-D simulation is 0.92, which is in excellent agreement with the experimental value shown in Fig. 1. The 2-D simulation, however, predicts a base suction pressure coefficient of 1.24, which overestimates the experimental value by as much as 38%. The solid line drawn in Fig. 1 extends the log-linear behavior of the base pressure coefficient obtained from experimental measurements in the unsteady two-dimensional regime ($49<\mathrm{Re}<180$), into the three-dimensional regime. It is interesting to note that the prediction of the base-pressure coefficient from the current 2-D simulation lies close to this line, indicating a continuous increase in the base suction pressure and drag with the Reynolds number if the flow were to remain two dimensional beyond $\mathrm{Re}=180$. An interesting related question is whether the increase in base suction pressure with a Reynolds number will saturate, and if so, then at what Reynolds number. Although the single data point obtained from the present simulation does not provide a conclusive answer, it at least shows that the trend of increase in base suction pressure with Reynolds number stays the same at least until $\mathrm{Re}^*=525$.

In Figs. 12(a) and 12(b) we have shown the streamlines corresponding to the mean flow obtained from the 2-D and 3-D simulations, respectively. A comparison of these figures shows that there are significant differences in the two flow fields. In the 2-D simulation, two pairs of large secondary vortices can be observed, and the streamline pattern matches

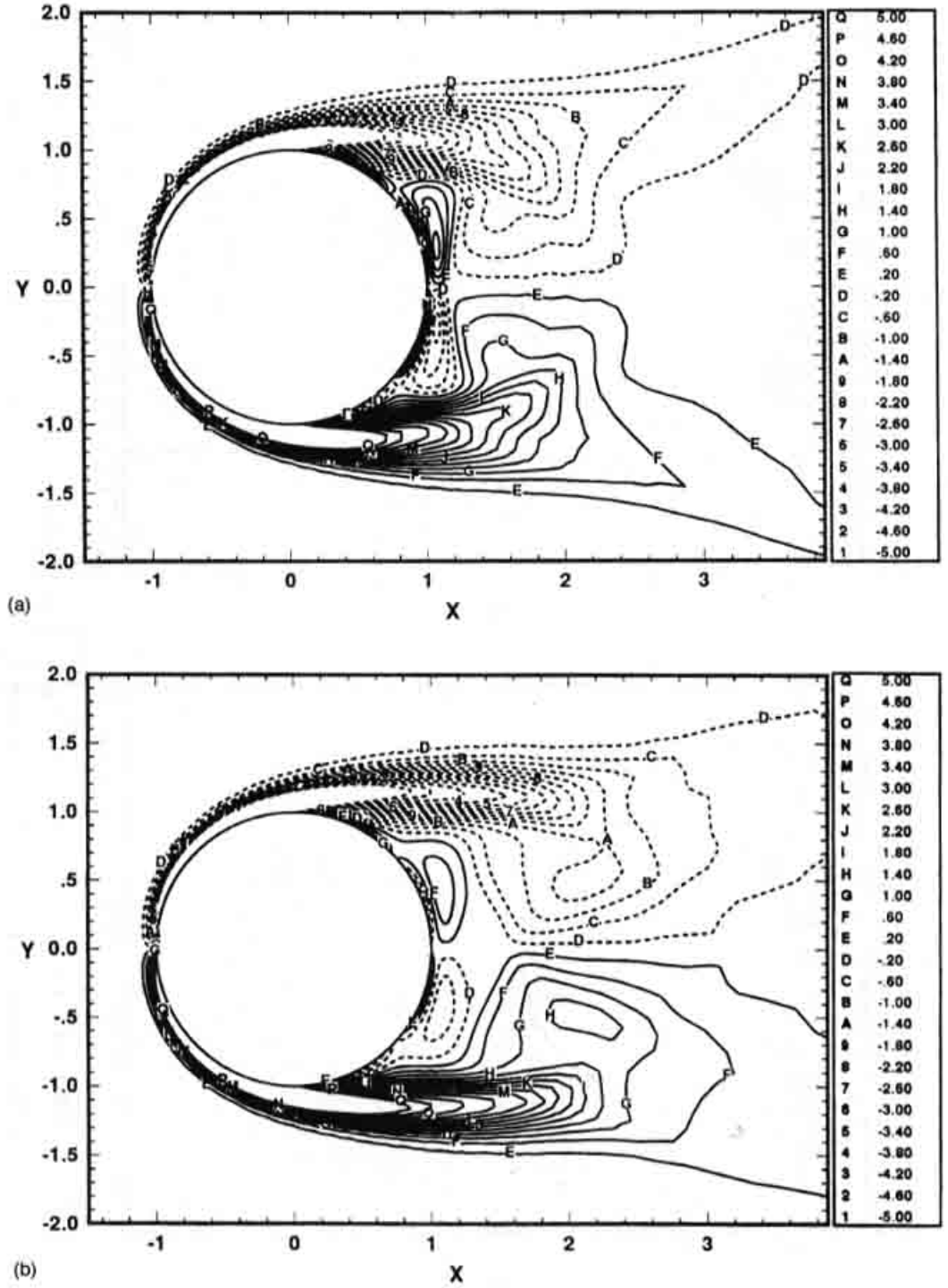

FIG. 9. Contours of $\bar{\omega}_z$ for the 2-D simulation of Case II. Solid and dashed contour lines correspond to positive and negative values, respectively. (b) Contours of $\bar{\omega}_z$ for the 3-D simulation of Case II. Solid and dashed contour lines correspond to positive and negative values, respectively.

well with the one obtained by Tamura *et al.*[6] at $Re^*=500$ [shown in Fig. 10(c) of their paper]. Streamlines corresponding to the mean flow for the 3-D simulation in Fig. 12(b) only show one pair of smaller secondary vortices. Also noticeable is the difference in the length of the recirculating bubble for the two simulations. For the 2-D simulation, the hyperbolic fixed point that denotes the downstream end of the recirculation bubble lies at about $x=2$, whereas for the 3-D simulation it lies at $x=2.65$.

3. Case III

The geometric parameters for this case have been chosen so that direct comparison of the results with the previous cases can shed some light on the effect of angle of attack and thickness ratio on the lift and drag for two-dimensional and three-dimensional flows.

Figures 13(a) and 13(b) show $\bar{\omega}_z$ for the 2-D and 3-D simulations, respectively, and it can be observed that there is

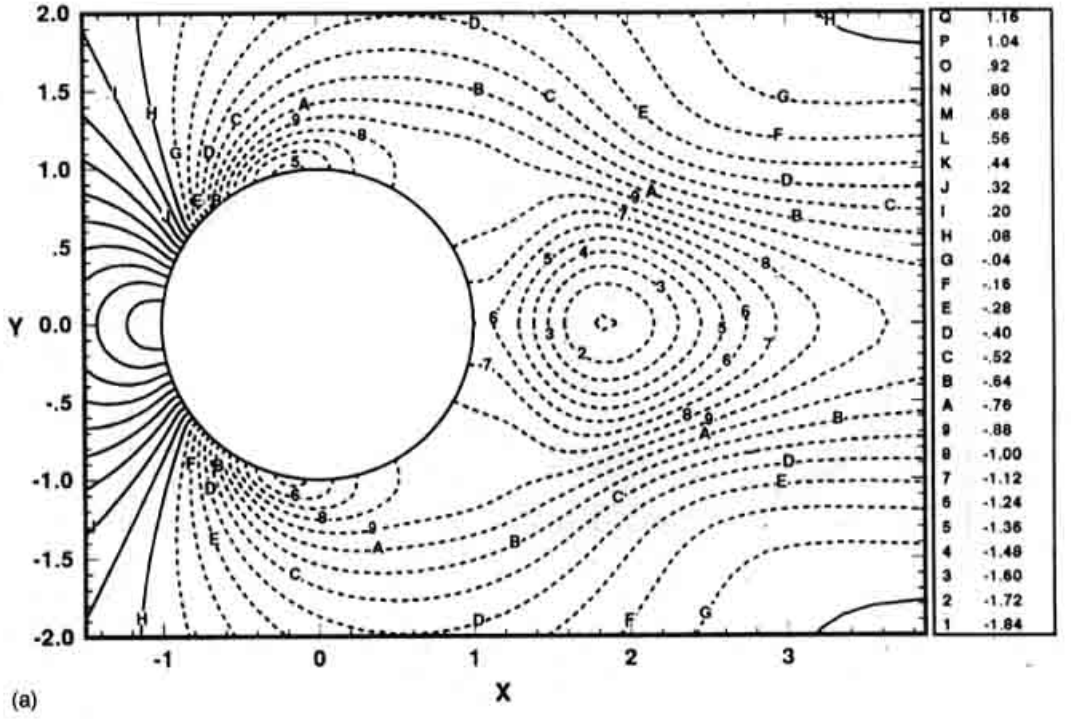

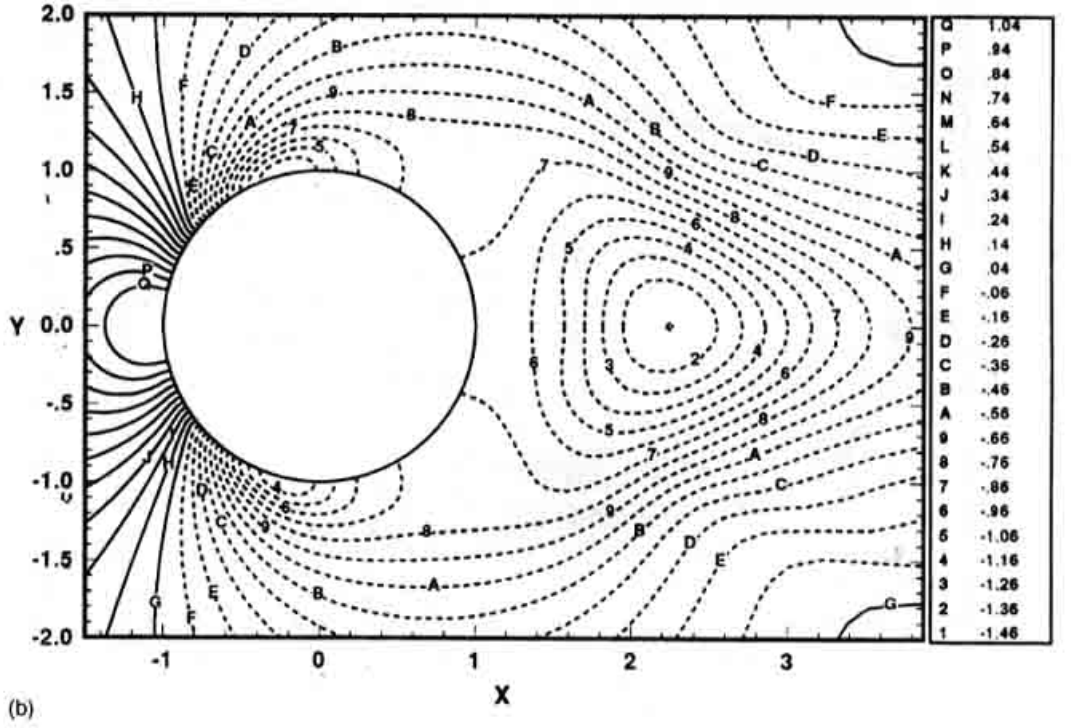

FIG. 10. (a) Contours of mean pressure coefficient, $C_{\bar{p}}$, for the 2-D simulation of Case II. Solid and dashed contour lines correspond to positive and negative values, respectively. (b) Contours of mean pressure coefficient, $C_{\bar{p}}$, for the 3-D simulation of Case II. Solid and dashed contour lines correspond to positive and negative values, respectively.

little qualitative difference in the two vorticity fields. The center of the vortices are at nearly the same distance from the body for both flows, although the strength of the vortex is slightly higher for the 2-D simulation. It is also found that the pressure in the wake region is lower for the 2-D simulation, and the $C_{\bar{p}}$ distribution for both the 2-D and the 3-D simulations shown in Fig. 14 suggests that the overall wake structure is similar to what is observed for the previous case.

All of the above differences in the vorticity and pressure fields are not as substantial as what were observed in the case with angle of attack or the circular cylinder, and the overall differences in the surface pressure distribution shown in Fig. 11 are also small. This suggests that the effect of three-dimensionality on the drag at a given Reynolds number depends very much on the shape of the body. A bluffer body has a wider and more energetic wake and the flow in the

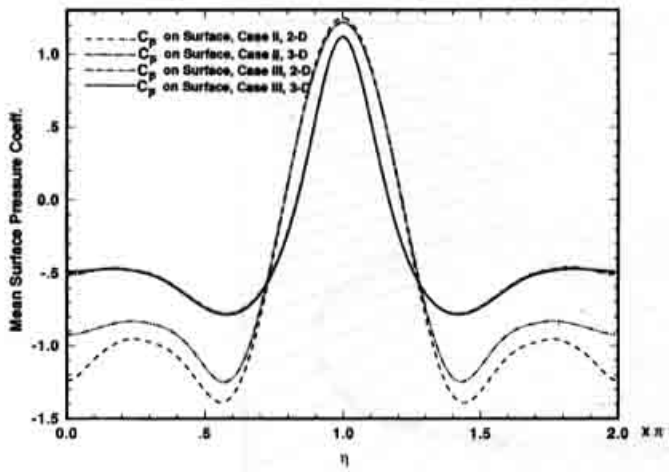

FIG. 11. Surface distribution of mean pressure coefficient, $C_{\bar{P}}$, for Cases II and III. Results of both 2-D and 3-D simulations have been plotted for comparison.

wake region has a much stronger influence on the surface pressure distribution. The elliptic cylinder at zero angle of attack is more streamlined compared to the cylinder at 45° angle of attack and a circular cylinder, thereby leading us to the conclusion that 2-D simulations of streamlined bodies, like for instance airfoils at low angles of attack, would lead to relatively accurate prediction of mean drag and lift forces.

B. Effect of the mean flow and Reynolds stresses on the mean drag and lift

As pointed out earlier, extrinsic three-dimensional effects are ruled out as a possible cause for the discrepancy between drag and lift forces computed from 2-D and 3-D simulations. Additional support for this conclusion can be found by noting that the current 3-D simulation of flow over a circular cylinder, which does not allow for any extrinsic three-dimensional effects, predicts the mean drag and the base suction pressure coefficient accurately. Thus, the discrepancy in the aerodynamic forces computed from 2-D and 3-D simulations is solely due to intrinsic three-dimensional effects. In this section we will explore the various intrinsic three-dimensional mechanisms that are conjectured to be the cause for the overprediction of drag in 2-D simulations, with the objective of clearly showing as to which of these mechanisms are mainly responsible for the overprediction.

The importance of time- and spanwise-averaged mean flow field on the mean surface pressure distribution on a circular cylinder has been addressed by Tamura *et al.*[6] They have argued that the differences in the mean flow obtained from the 2-D and 3-D simulations are primarily responsible for the differences in the base pressure distribution and in the lift and drag forces. In particular, the strong secondary eddies observed in the mean flow pattern of the 2-D simulations have been conjectured to be the primary cause of increased drag forces. In addition to this, rapid roll-up of the Kármán vortices close to the cylinder is also thought to be the cause of a lower pressure in the wake for 2-D simulations.[1]

On the other hand, Sychev[9] suggested that inside the wake, pressure is roughly in equilibrium with the shear stresses. On this basis, Roshko[6] has argued that for sufficiently high Reynolds numbers, base suction pressure is determined mainly by the velocity perturbations away from the mean through the action of Reynolds stresses in the wake. Furthermore, he has used this information in conjunction with a simple control volume analysis of the mean wake and obtained a relation between the base pressure, the mean shear stress in the separated region, and the length and width of the wake.

These viewpoints are not necessarily contradictory. From an equation for the mean flow it can be clearly seen that differences in the mean flow between the 2-D and 3-D simulations are indeed the result of differences in their Reynolds stresses. On the other hand, in Roshko's[6] analysis, the direct influence of the mean flow enters through the length and width of the wake. Therefore the Reynolds stresses affect the mean pressure distribution both directly and also indirectly through the mean flow. The present simulations provide us with an opportunity to isolate the action of these two effects on the mean pressure distribution and investigate the relevant physical mechanisms in greater detail. The relative importance of mean flow and Reynolds stresses in determining the mean pressure distribution is of interest since it is not clear whether an accurate prediction of mean flow alone could guarantee accurate prediction of the mean lift and drag forces.

We begin by considering the pressure Poisson equation, given by

$$\nabla^2 P = -\nabla\cdot(\mathbf{u}\cdot\nabla\mathbf{u}), \quad \text{in } \Omega, \tag{3}$$

$$\tilde{\xi}\cdot\nabla P = \tilde{\xi}\cdot\left(\frac{1}{\mathrm{Re}}\nabla^2\mathbf{u} - (\mathbf{u}\cdot\nabla\mathbf{u})\right), \quad \text{on } \partial\Omega, \tag{4}$$

where Ω refers to the computational volume, $\partial\Omega$ denotes the boundary of the computational domain (which includes the body surface as well as the outer boundary), and $\tilde{\xi}$ is the unit vector normal to the boundary of the computational domain. At Reynolds numbers considered in this study, the effect of the boundary condition on the pressure is small, and for the most part, the pressure is determined by the source term of the pressure Poisson equation.

The influence of the mean flow and the Reynolds stresses on the mean pressure distribution can now be evaluated by decomposing the source term into a contribution from the mean flow and a contribution from the Reynolds stresses. Correspondingly, the mean pressure can be decomposed into two components, i.e., $\bar{P} = \bar{P}_m + \bar{P}_{rs}$, which are given by

$$\frac{\partial^2\bar{P}_m}{\partial x^2} + \frac{\partial^2\bar{P}_m}{\partial y^2} = -\left(\frac{\partial^2\bar{u}^2}{\partial x^2} + 2\frac{\partial^2\bar{u}\,\bar{v}}{\partial x\,\partial y} + \frac{\partial^2\bar{v}^2}{\partial y^2}\right), \quad \text{in } \Omega, \tag{5}$$

which is solved with the following boundary condition:

$$\tilde{\xi}\cdot\nabla\bar{P}_m = \tilde{\xi}\cdot\left(\frac{1}{\mathrm{Re}}\nabla^2\bar{\mathbf{u}} - (\bar{\mathbf{u}}\cdot\nabla\bar{\mathbf{u}})\right), \quad \text{on } \partial\Omega \tag{6}$$

and

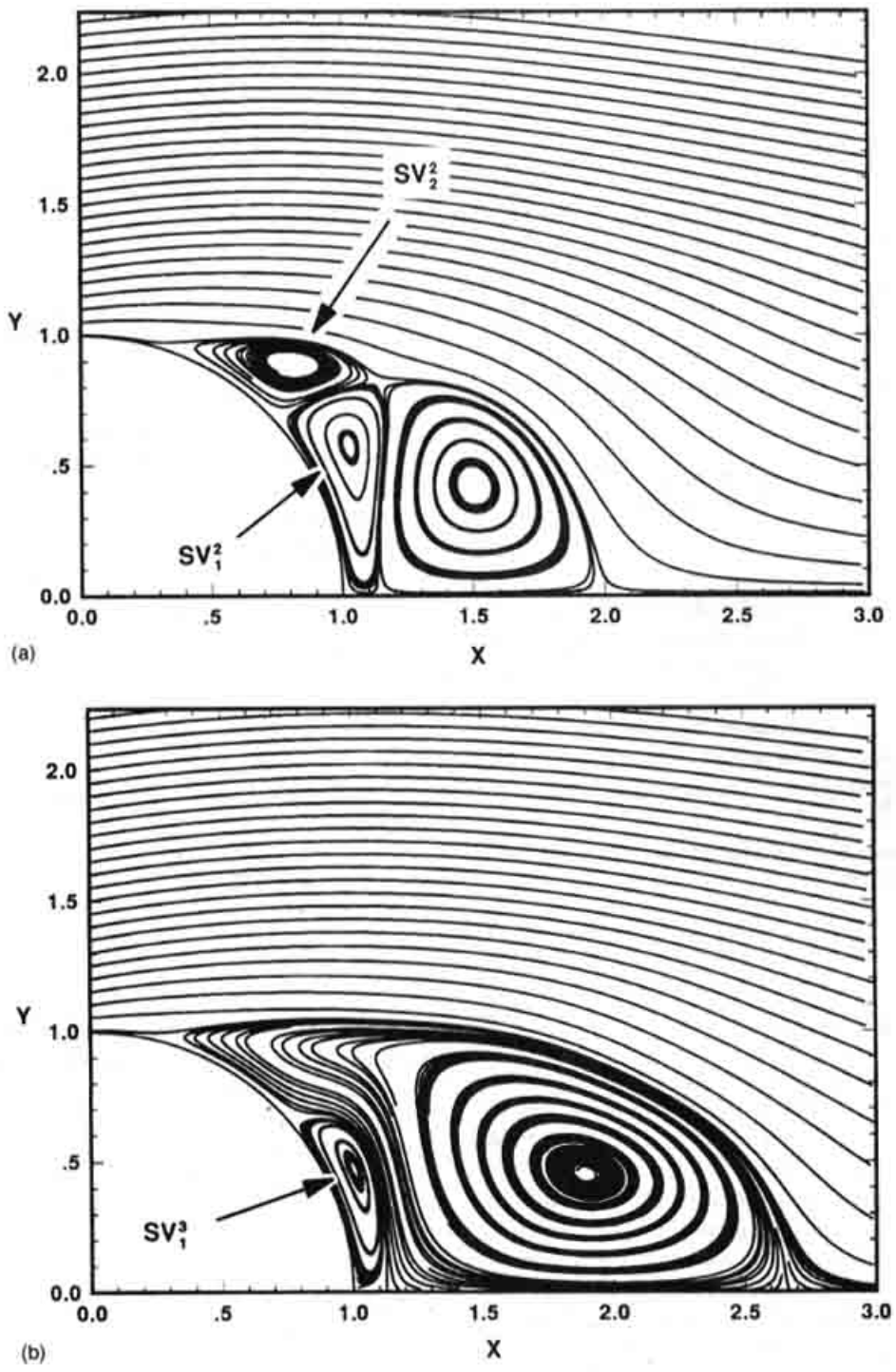

FIG. 12. (a) Mean streamline pattern for the 2-D simulation of Case II, which shows the presence of two secondary vortices in addition to the primary vortex. The secondary vortices has been labeled so that correlation can be made with the surface pressure distribution. (b) Mean streamline pattern for the 3-D simulation of Case II, which shows the presence of one secondary vortex in addition to the primary vortex. The location of this secondary vortex has also been marked.

$$\frac{\partial^2 \tilde{P}_{rs}}{\partial x^2}+\frac{\partial^2 \tilde{P}_{rs}}{\partial y^2}=-\left(\frac{\partial^2 \overline{u'^2}}{\partial x^2}+2\,\frac{\partial^2 \overline{u'\,v'}}{\partial x\,\partial y}+\frac{\partial^2 \overline{v'^2}}{\partial y^2}\right),\quad \text{in } \Omega, \tag{7}$$

for which the boundary condition is given by

$$\tilde{\xi}\cdot\nabla \tilde{P}_{rs}=-\tilde{\xi}\cdot(\overline{\mathbf{u}'\cdot\nabla\mathbf{u}'}),\quad \text{on } \partial\Omega. \tag{8}$$

In the above equations $\tilde{P}_m$ is the contribution to mean pressure from the mean flow and $\tilde{P}_{rs}$ is the direct contribution of the Reynolds stresses to the mean pressure. Here u and v are the Cartesian velocity components along the x (streamwise) and y (cross-flow) directions, respectively, where the stream-

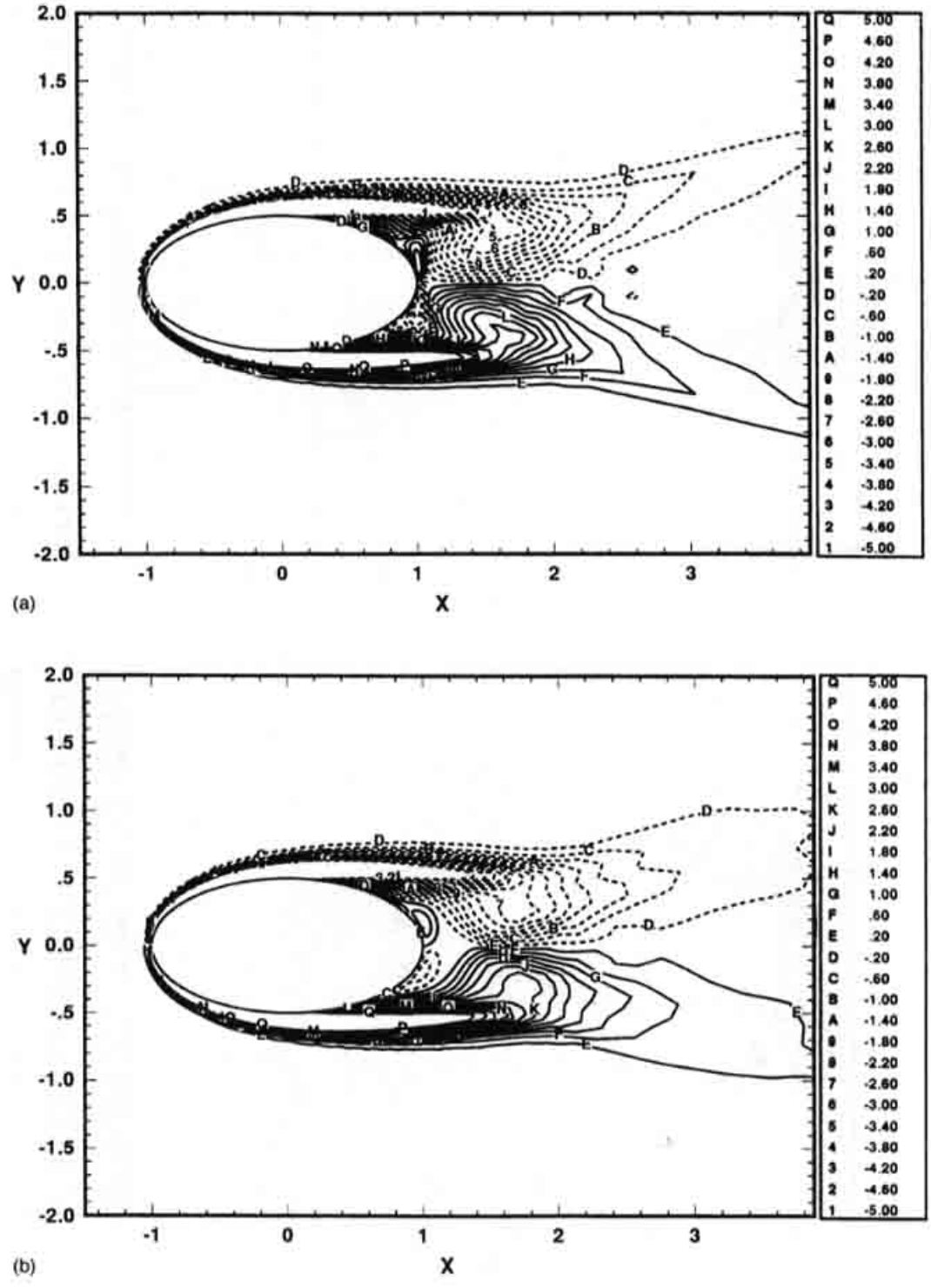

FIG. 13. (a) Contours of $\bar{\omega}_z$ for the 2-D simulation of Case III. Solid and dashed contour lines correspond to positive and negative values, respectively. (b) Contours of $\bar{\omega}_z$ for the 3-D simulation of Case III. Solid and dashed contour lines correspond to positive and negative values, respectively.

wise direction denotes the direction of the free-stream (see Fig. 3). Note that each of the the above pressure Poisson equations are formulated so as to individually satisfy the compatibility condition, however, we find that since the outer boundary is sufficiently far away from the body, the boundary condition at the outer boundary has a negligible effect on the above pressure computations.

It can be seen from the above equations that the spanwise velocity perturbations and the associated Reynolds stress components do not affect the mean pressure directly. However, the importance of these stress components cannot be understated, since it is these stress components that alter the in-plane stress components, which, in turn, modify the mean flow and the mean pressure distribution. It should be noted that the above decomposition is analogous to the decomposition of pressure into "fast" and "slow" components in a turbulent flow.

In what follows, we will present the contribution to the

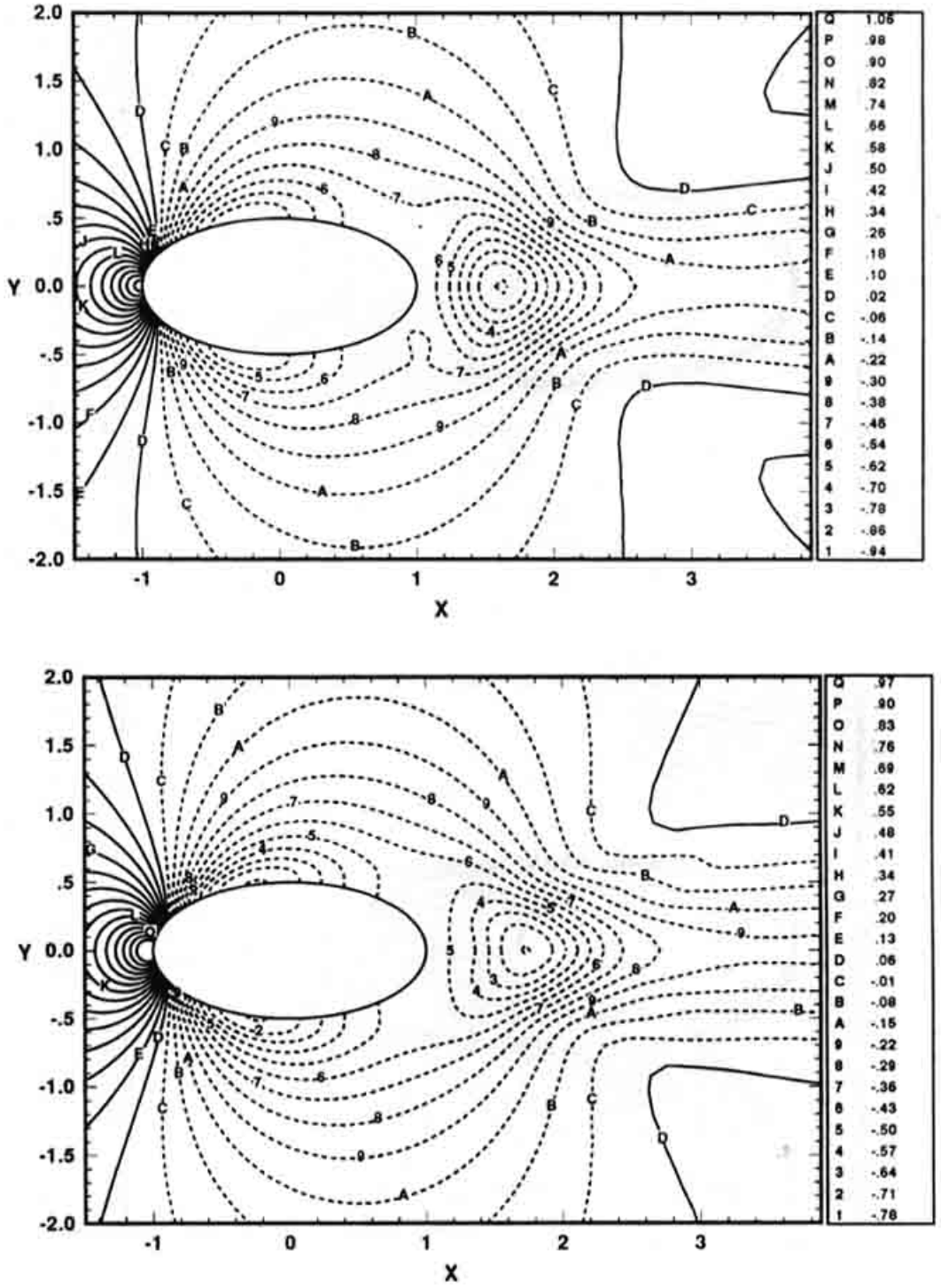

FIG. 14. (a) Contours of mean pressure coefficient, $C_{\bar{p}}$, for the 2-D simulation of Case III. Solid and dashed contour lines correspond to positive and negative values, respectively. (b) Contours of mean pressure coefficient, $C_{\bar{p}}$, for the 3-D simulation of Case III. Solid and dashed contour lines correspond to positive and negative values, respectively.

mean pressure from the mean flow and in-plane Reynolds stresses for the three different cases considered in this study. Figures 15(a) and 15(b) show contours of Reynolds shear stress, $\overline{u'v'}$, for the 2-D and 3-D simulations of Case I, respectively. It is observed that the maximum magnitude of the Reynolds shear stress in the 2-D simulation is about 0.23, which is roughly twice the corresponding value in the 3-D simulation. Thus, the Reynolds shear stress produced in the 2-D simulation is significantly larger than that of the 3-D simulation. This is in line with the observations of Williamson and Roshko,[2] who reports a reduction in the measured Reynolds shear stress with increasing three-dimensionality in the circular cylinder wake over a Reynolds number range of 260 to 1500. In 2-D simulations, all the energy extracted from the mean flow field is expended in sustaining the in-plane velocity fluctuations. However, in 3-D simulations,

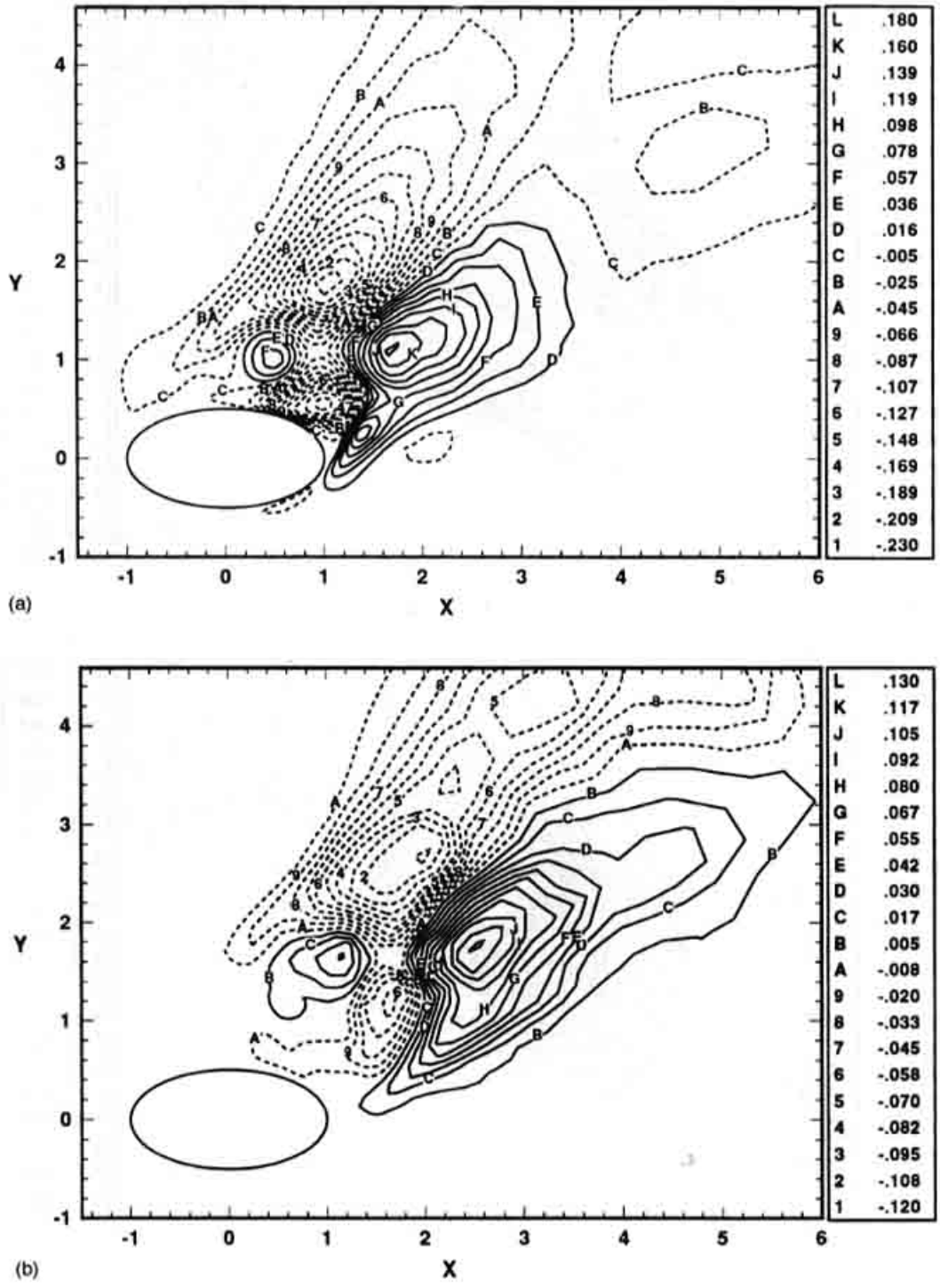

FIG. 15. (a) Contours of Reynolds shear stress, $\overline{u'v'}$, obtained from the 2-D simulation of Case I. Solid and dashed contour lines correspond to positive and negative values, respectively. (b) Contours of Reynolds shear stress, $\overline{u'v'}$, obtained from 3-D simulation of Case I. Solid and dashed contour lines correspond to positive and negative values, respectively.

part of the energy extracted from the mean flow is used up in maintaining spanwise velocity fluctuations, thereby leading to a reduction in the intensity of the in-plane velocity fluctuations and consequently the in-plane Reynolds stress components. It is also important to note that in addition to a higher magnitude, the region of intense Reynolds shear stress also lies closer to the cylinder in the 2-D simulations.

As evident from Eq. (7), in addition to the in-plane Reynolds shear stress, the in-plane Reynolds normal stresses also affect the mean pressure in the wake. Figures 16(a) and 16(b) show the streamwise ($\overline{u'^2}$) and cross-flow ($\overline{v'^2}$) Reynolds normal stress distributions, respectively, which have been obtained from the 3-D simulation. It can be seen that the magnitudes of both these stresses are larger than the Rey-

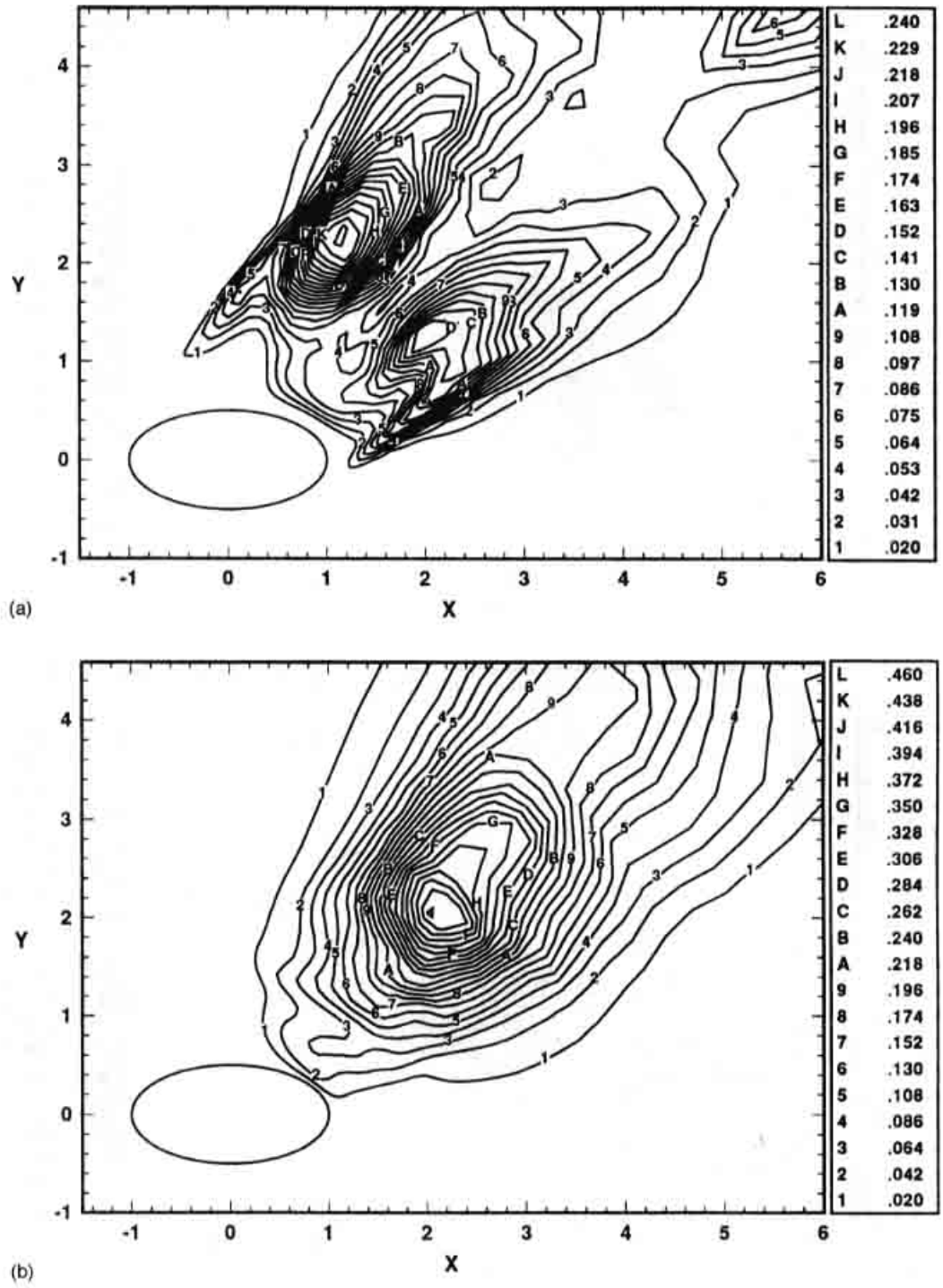

FIG. 16. (a) Contours of streamwise Reynolds normal stress, $\overline{u'^2}$, obtained from 3-D simulation of Case I. (b) Contours of cross-flow Reynolds normal stress, $\overline{v'^2}$ obtained from 3-D simulation of Case I.

nolds shear stress, and thus the normal stresses also have a significant effect on the pressure in the wake.

Figures 17(a) and 17(b) show the Reynolds shear stress distribution for the circular cylinder (Case II) obtained from 2-D and 3-D simulations, respectively. As in Case I, it is found that the Reynolds shear stress in the 2-D simulation is significantly higher than in the 3-D simulation. In both these figures (and in subsequent figures as well) the separating streamlines for the mean flow have been plotted so that the correspondence between the Reynolds stresses and the mean flow can be clearly seen. Roshko[4] has proposed a wake model for bluff bodies in the absence of vortex shedding, such as those with a long splitter plate in the wake, which assumes that the maximum Reynolds shear stress occurs in the shear layers at the top and bottom boundaries of the mean recirculating bubble. The model is successful in predicting the base pressure in the absence of shedding with a simple balance of shear stresses and pressure in the mean wake

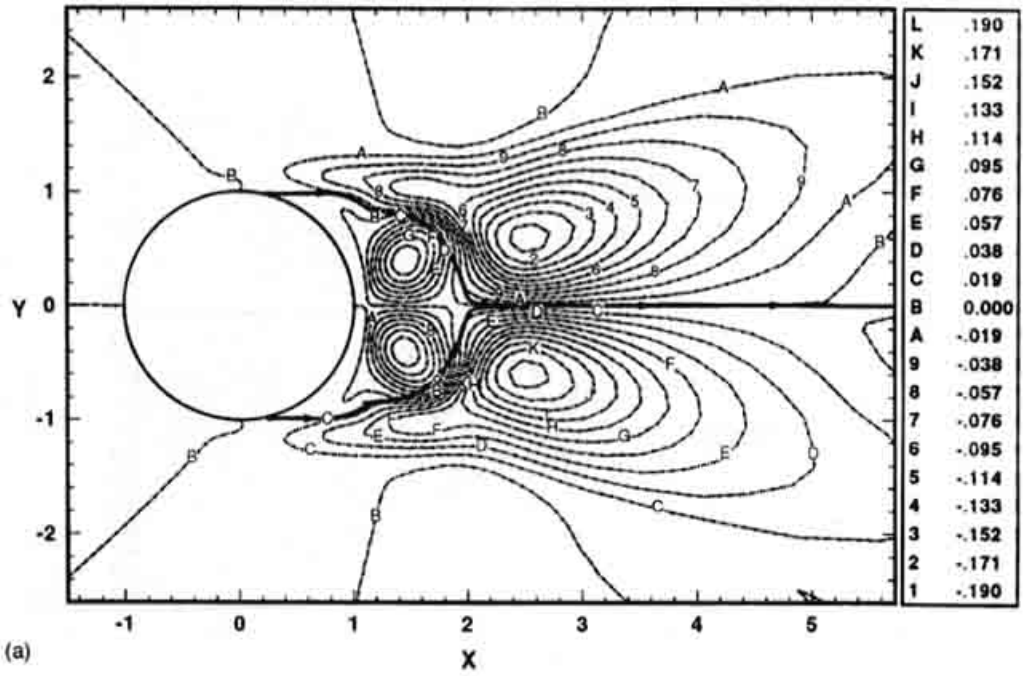

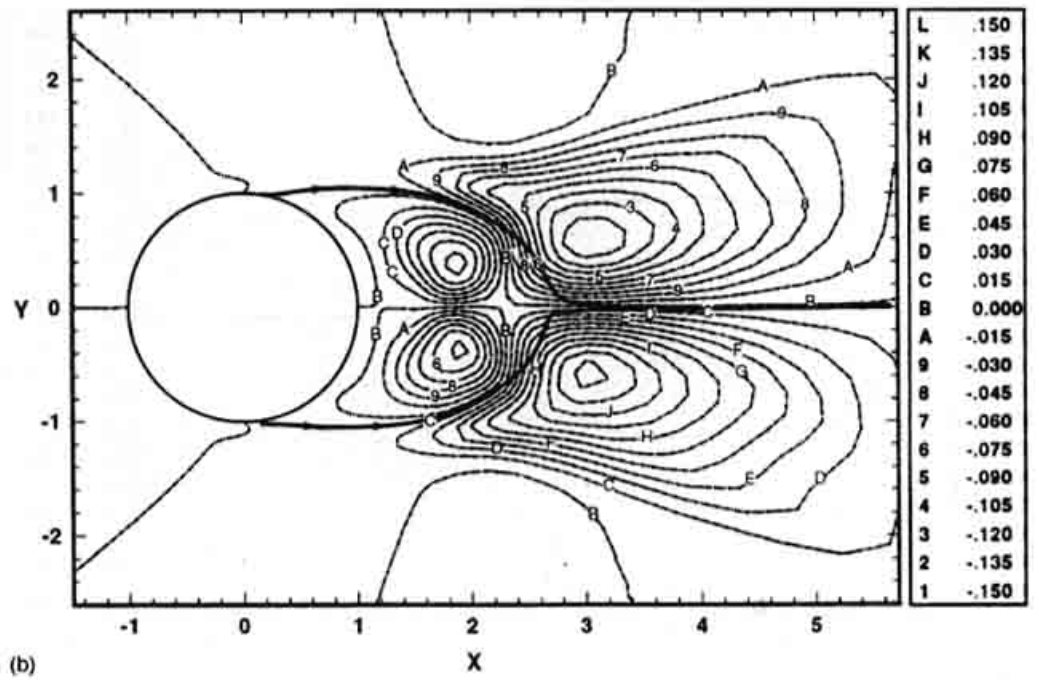

FIG. 17. (a) Contours of Reynolds shear stress, $\overline{u'v'}$, obtained from the 2-D simulation of Case II. The mean separating streamline has also been shown by a bold line so that the stress distribution can be seen in relation to the mean separation bubble. (b) Contours of Reynolds shear stress, $\overline{u'v'}$, obtained from 3-D simulation of Case II. The mean separating streamline is also shown.

bubble. It has also been pointed out that this model is invalid for wakes where shedding is present, since experimental results[22] show that the Reynolds shear stresses attain large values not on the mean separating streamlines but inside the separation bubble. From Fig. 17 we find that indeed the Reynolds shear stress is not maximum on the separating streamline, in fact, the Reynolds shear stress is small everywhere on the separating streamline, and the separating streamline seems to coincides well with the zero Reynolds shear stress contour (contour labeled "B") in Fig. 17(b).

The Reynolds normal stresses shown in Figs. 18(a) and 18(b) for the 3-D simulation are also found to be significantly higher in magnitude than the corresponding shear stress. While both the normal stresses are symmetric about $\eta=0$, the streamwise Reynolds normal stress, $\overline{u'^2}$, reach a local minimum and the cross-flow Reynolds normal stress, $\overline{v'^2}$, reaches a local maximum along the line of symmetry. It is also worth pointing out that the Reynolds shear and normal stress distributions agree qualitatively with the results

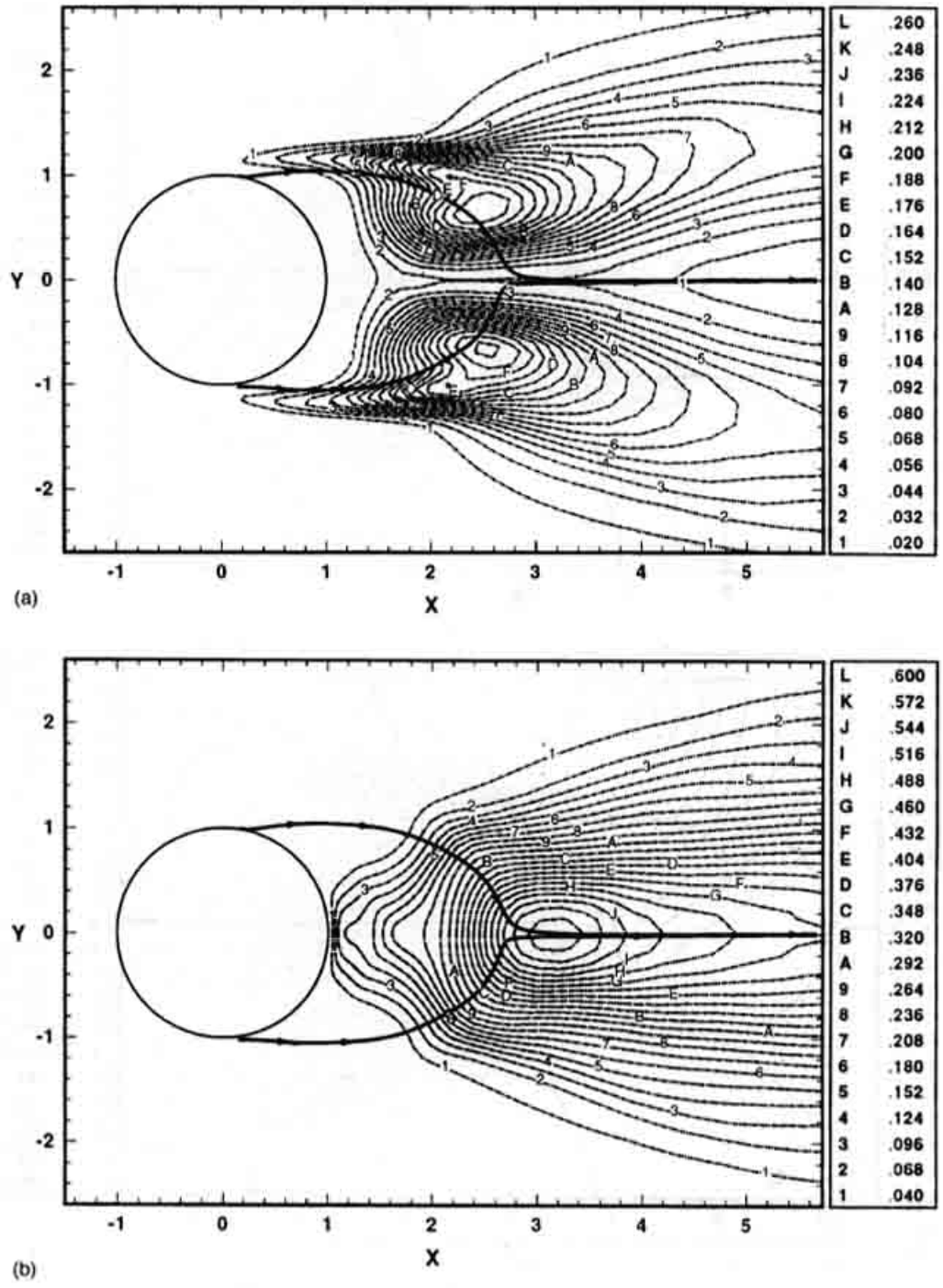

FIG. 18. (a) Contours of streamwise Reynolds normal stress, $\overline{u'^2}$, obtained from 3-D simulation of Case II. The mean separating streamline is also shown. (b) Contours of cross-flow Reynolds normal stress, $\overline{v'^2}$, obtained from 3-D simulation of Case II. The mean separating streamline is also shown.

of Henderson[23] for a circular cylinder, although some differences in the location of the stress extremas can be observed. The stress distribution obtained here is also in qualitative agreement with the observations of Cantwell and Coles[22] for a flow over a circular cylinder at a large Reynolds number of 140 000.

In Figs. 19(a) and 19(b), contours of the pressure coefficient corresponding to $\bar{P}_m$ and $\bar{P}_{rs}$ for the 3-D simulation of Case II have been plotted along with the separating streamlines. For $\bar{P}_m$ we observe that the lowest pressure is attained on the top and bottom portions of the cylinder surface. However, $\bar{P}_{rs}$ exhibits a region of high suction in the wake region, which is located close to the hyperbolic fixed point that defines the downstream end of the recirculating bubble. It can be observed that the Reynolds stress contribution to pressure increases to P_∞ downstream of this region of high suction. On the cylinder surface, it takes small negative values in the wake region, but is close to P_∞ in the upstream section of the cylinder. On the other hand, mean flow contribution to the mean pressure shows strong variations in the vicinity of the cylinder.

The surface variation of $\bar{P}_m$ and $\bar{P}_{rs}$ coefficients for this

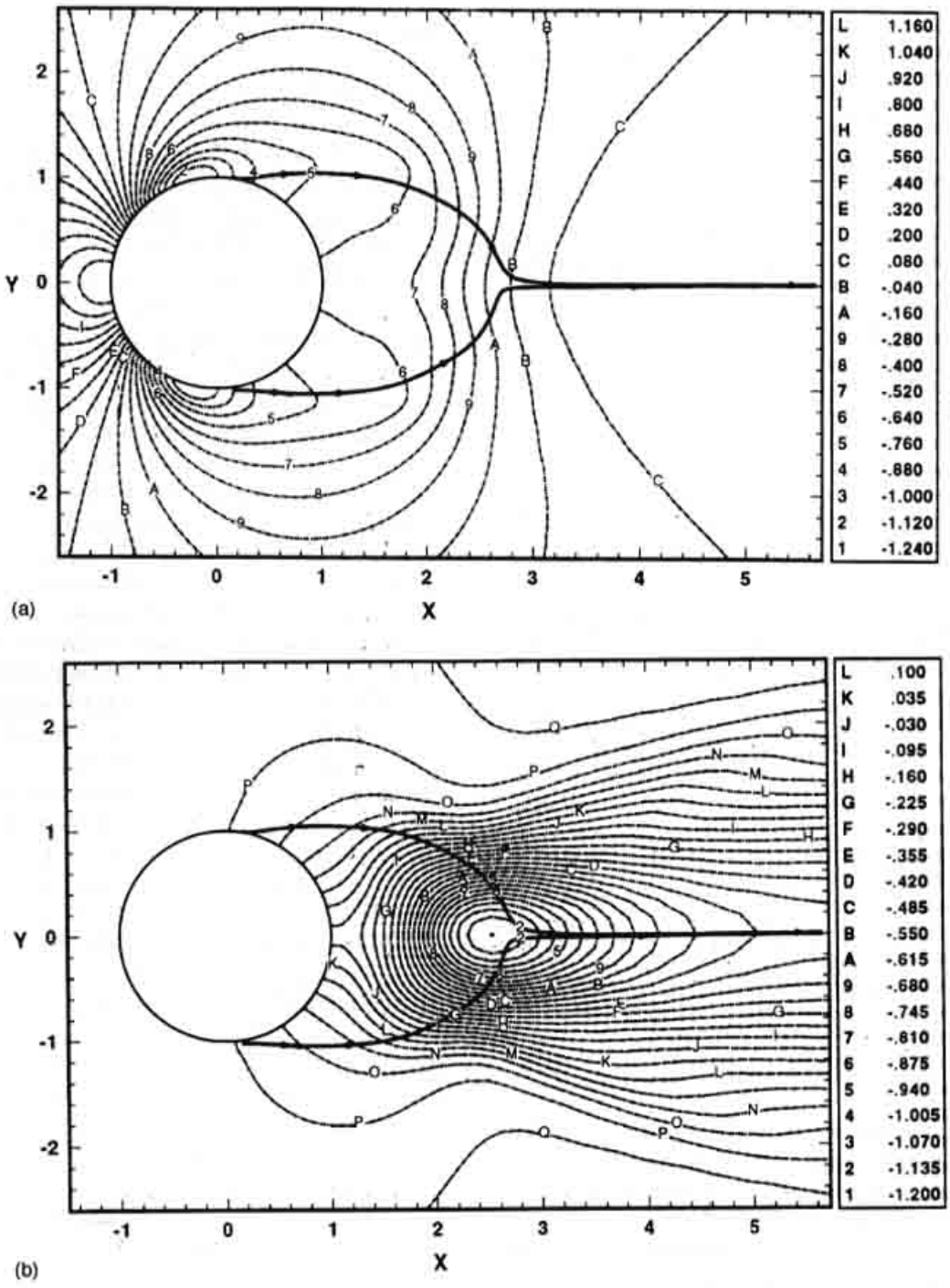

FIG. 19. (a) Contours of coefficient of $\tilde{P}_m$ obtained from 3-D simulation of Case II. The mean separating streamline is also shown. (b) Contours of coefficient of $\tilde{P}_{rs}$ obtained from 3-D simulation of Case II. The mean separating streamline is also shown.

case of a circular cylinder is shown in Fig. 20(a), where the results for the 2-D simulation have also been plotted. The largest contribution to mean pressure is from the mean flow, and differences between two-dimensional and three-dimensional surface pressure distributions are limited to the wake region. While the mean front stagnation pressure remains the same for both the 2-D and 3-D simulations, $\tilde{P}_m$ for the 2-D simulation reaches larger suction values near the top and bottom separation points and recovers to a slightly lower suction value in the base. The net difference in drag due to $\tilde{P}_m$ between 2-D and 3-D simulations is only mild. On the other hand, the stronger Reynolds stresses being closer to the cylinder in the 2-D simulation cause strong suction values of $\tilde{P}_{rs}$, resulting in increased drag. It should be pointed out that it is actually the gradients of the Reynolds stresses that directly effect the pressure distribution [see Eq. (7)], however, since the Reynolds stresses are constrained to be zero on the cylinder surface, a higher level of Reynolds stresses in the wake, in general, leads to higher gradients of the Reynolds stresses. Thus, it is reasonable to associate higher suction pressure directly with a higher level of Reynolds stresses in the wake.

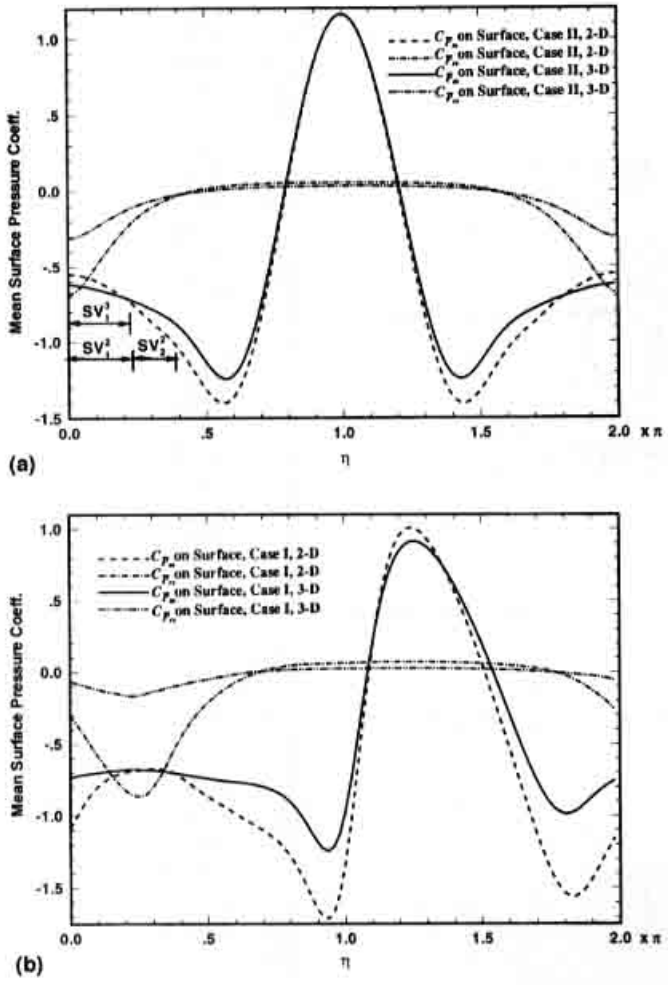

FIG. 20. (a) Surface distribution of coefficients of $\bar{P}_m$ and $\bar{P}_{rs}$ for Case II obtained from 2-D and 3-D simulations. (b) Surface distribution of coefficients of $\bar{P}_m$ and $\bar{P}_{rs}$ for Case I obtained from 2-D and 3-D simulations. The angular extent of the secondary vortices marked in Fig. 12 is shown in the figure.

Table II lists the contribution of the two pressure components ($\bar{P}_m$ and $\bar{P}_{rs}$) to the pressure drag for all the three cases considered in this study. A number of observations can be made from this table.

(1) It has been noted before that the overprediction of the total drag by 2-D simulations is larger for bluffer bodies. It is interesting to note from the above table (and Table I) that the pressure drag and skin-friction drag show the same trend. In fact, we find that both the pressure drag and skin-friction drag are overpredicted by about the same percentage as the total drag (39%, 16%, and 1% for the three cases, respectively).

(2) In 2-D simulations the contribution of the Reynolds stress components to the mean pressure drag is relatively small at about 35%, 31%, and 13%, respectively, for the three cases, and furthermore, this contribution is even smaller for the corresponding 3-D simulations (10%, 17%, and 12%, respectively). In Fig. 20(a) the surface distributions of $\bar{P}_m$ and $\bar{P}_{rs}$ coefficients for the circular cylinder are plotted for both the 2-D and 3-D simulations together for comparison, and the corresponding plot for Case I is shown in Fig. 20(b). From these figures it can be seen that, especially for the 3-D simulations, the effect of the Reynolds stresses on the surface pressure is confined to the wake region, and even there, this effect is small compared to that of the mean flow. This implies that the direct effect of the Reynolds stresses on the mean pressure is small, and consequently, a major portion of the pressure drag is determined by the mean velocity field.

(3) Despite the significant differences in the surface distribution of $\bar{P}_m$ obtained from 2-D and 3-D simulations (see Fig. 20), it is noted from Table II that the drag due to this component of pressure changes by only a small amount (less than 3%), ingoing from a 2-D to a 3-D simulation for all the cases studied here. As seen in Fig. 20, the differences in $\bar{P}_m$ obtained from 2-D and 3-D simulations are significant only near the top and bottom separation points, however, the contribution to drag from the surface pressure in these regions is small due to the local orientation of the cylinder surface. Thus, for the geometries considered in this study, the differences observed in the mean flow between the 2-D and 3-D simulations have little impact on the overall drag coefficient. On the other hand, for extremely bluff bodies, like, for instance, a normal flat plate, the local orientation of the surface is everywhere in the streamwise direction, and therefore we expect that differences in $\bar{P}_m$ will make a more significant contribution to the overall difference in the drag.

(4) The increased drag in 2-D simulations is primarily due to the differences in the Reynolds stress portion of the pressure drag (see Table II). It can be seen in Fig. 20 that large Reynolds stresses in 2-D simulations lead to an increase in the base suction pressure. It is interesting to note that the local minimum in the surface pressure distribution for the 2-D simulation of Case I located at around $\eta=0.25\pi$ shown in Fig. 7, can be attributed directly to the minimum in $\bar{P}_{rs}$ at the same location [Fig. 20(b)]. No such minimum is observed in the 3-D simulations, and thus this minimum can

TABLE II. Various components of pressure drag for the three cases considered in this study.

	2-D			3-D		
Case No.	Pressure drag coefficient	Mean flow contribution	Re stress contribution	Pressure drag coefficient	Mean flow contribution	Re stress contribution
I	2.26	1.48	0.78	1.62	1.46	0.16
II	1.27	0.87	0.40	1.09	0.90	0.19
III	0.58	0.50	0.08	0.57	0.50	0.07

be considered a spurious feature since it would not be observed in a "real" laboratory flow.

Since $\bar{P}_m$ is the pressure due to the mean flow field, any effect of the secondary vortices observed in the case of the circular cylinder should be apparent in the surface distribution of $\bar{P}_m$ shown in Fig. 20(a). The secondary vortices have been labeled in Figs. 12(a) and 12(b), and the corresponding location of these vortices are marked in Fig. 20(a). A closer look at the distribution of $\bar{P}_m$ in these regions reveals that the presence of the secondary vortices does not have any noticeable effect on the surface pressure distribution. Therefore, it seems that the presence of the secondary vortices does not have any direct bearing on the overprediction of drag in 2-D simulations.

The roll-up of the vortices closer to the cylinder in 2-D simulations results in the region of high Reynolds stresses being closer to the cylinder. This enhances the effect of the Reynolds stresses on the surface pressure, and leads to a higher base suction pressure in 2-D simulations. Thus, the effect of a smaller wake length in the 2-D simulations on the surface pressure, and hence the drag, is felt primarily through the Reynolds stresses, and only to a lesser extent through the mean flow. However, as mentioned earlier, for a bluffer body like a normal flat plate, the mean flow will play a more significant role in the overprediction of drag and the effect of a smaller wake length might be felt directly from the mean flow field.

Thus, 2-D simulations have a tendency to overemphasize the effect of in-plane Reynolds stresses on the surface pressure distribution, and this seems to be the main cause for overprediction of drag in 2-D simulations for all the cases studied here. It should be reiterated here that the differences between the mean flow obtained from 2-D and 3-D simulations are themselves due to the differences in the Reynolds stresses. Therefore, the differences in $\bar{P}_m$ between the two simulations can be regarded as an indirect effect of the differences in the Reynolds stresses. However, in simulations where extrinsic three-dimensional effects (like end effects, spanwise variation of inflow, spanwise varying shape of the body, etc.) are present, differences between the mean flow obtained from 2-D and 3-D simulations cannot be attributed totally to the change in the Reynolds stresses, and this adds an extra level of complexity to the analysis.

For a 3-D simulation of Case I, it is found that the coefficient of lift due to $\bar{P}_m$ and $\bar{P}_{rs}$ are 0.84 and 0.04, respectively. Thus, the mean pressure due to the Reynolds stresses contributes only about 5% to the total lift for the 3-D simulations, and this implies that the lift is determined for the most part by the mean flow, and we believe that the relatively small difference in lift between the 2-D and 3-D simulations (11% overprediction in lift as compared to 39% in drag) is connected to the difference in the vorticity production in the unseparated boundary layer region upstream of the wake (Fig. 7).

C. Peak-to-valley amplitude of fluctuating lift and drag

It is observed that there is gross overprediction of the peak-to-valley amplitude levels of lift in 2-D simulations for all the three cases. This phenomenon has not received much attention in previous studies, although a study of flow over square cylinders by Sakamoto *et al.*[24] did find that 2-D simulations overpredict the frequency of the lift and drag fluctuations. Correct prediction of the level of fluctuation of the aerodynamic forces is important, since structures are usually designed with the maximum load in mind, and thus one needs to be able to predict the peak aerodynamic loads on the structure. Furthermore, the amplitude of the aerodynamic loads is important in the study of resonant fluid–structure interaction.

To gain insight into this phenomena, we have resorted to a triple decomposition of the flow variables.[22,25] For a variable f, the decomposition is given by

$$f(\xi,\eta,z,t)=\bar{f}(\xi,\eta)+f^{\mathfrak{P}}(\xi,\eta)e^{i(2\pi t/T)}+\text{c.c.} +f''(\xi,\eta,z,t), \tag{9}$$

where the mean, $\bar{f}$, has been defined previously [see Eqs. (1) and (2)], and c.c. is the complex conjugate of the second term on the right-hand side. The second and third terms on the right-hand side of Eq. (9) make up the phase-averaged part of the variable, and thus the total phase-averaged part of the perturbation can be determined at any phase of the shedding cycle by evaluating the sum of these two terms. Furthermore, in the above decomposition, f'' corresponds to the fluctuation about the phase average. The mean- and the phase-averaged quantities will be referred to as the coherent portion of the variable, and the fluctuation f'' will be referred to as the incoherent portion of the variable. The amplitude of the phase-averaged part $f^{\mathfrak{P}}$, is, in general, complex and is defined as follows:

$$f^{\mathfrak{P}}(\xi,\eta)=\frac{1}{T}\frac{1}{L_z}\int_0^{L_z}\int_0^{T} f(\xi,\eta,z,t)e^{-i(2\pi t/T)}dt\,dz. \tag{10}$$

The above definition is for 3-D simulations and a corresponding definition for 2-D simulations does not require an average along the span. It should be pointed out that the last three terms on the right-hand side of Eq. (9) are together equal to the perturbation (f') away from the mean. Here the phase average, $f^{\mathfrak{P}}$, is defined to correspond to a pure sinusoidal component without any higher harmonics, and thus differs from the phase average defined by Cantwell and Coles.[22] At the moderate Reynolds number considered in this study, most of the energy is in the fundamental mode and the first harmonic, and only a small part of it is in the higher harmonics.

From the above definition, the pressure field can be decomposed into a mean pressure, $\bar{P}$, phase-averaged pressure, $P^{\mathfrak{P}}$, and an incoherent pressure fluctuation, P''. A pressure Poisson equation can be obtained for each of these components. In particular, for the purpose of investigating the large-scale fluctuation of lift on the cylinder, we seek a pressure Poisson equation for the phase-averaged portion of pressure. It is seen that $P^{\mathfrak{P}}$ receives contribution from both the coherent and the incoherent components of the velocity field, and

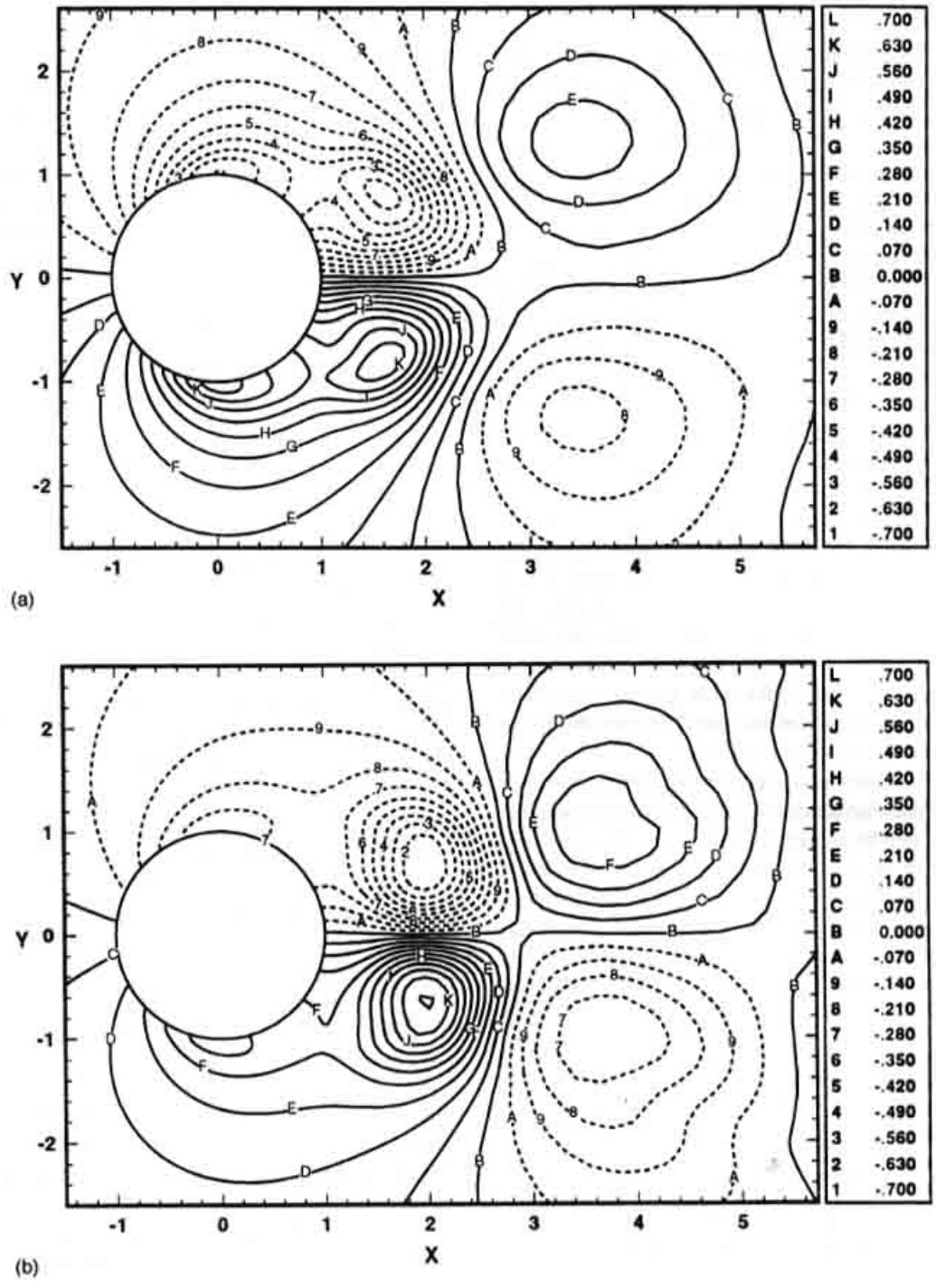

FIG. 21. (a) Phase-averaged pressure coefficient obtained from 2-D simulation of Case II. Phase is chosen to correspond to the instant of maximum lift. Solid and dashed contour lines correspond to positive and negative values, respectively. (b) Phase-averaged pressure coefficient obtained from 3-D simulation of Case II. Phase is chosen to correspond to the instant of maximum lift. Solid and dashed contour lines correspond to positive and negative values, respectively.

thus the phase-averaged pressure amplitude can be further decomposed into coherent and incoherent contributions as $P^{\Phi} = P_c^{\Phi} + P_i^{\Phi}$, where these two components are given by

$$\frac{\partial^2 P_c^{\Phi}}{\partial x^2} + \frac{\partial^2 P_c^{\Phi}}{\partial y^2} = -2\left(\frac{\partial^2[\tilde{u}u^{\Phi}]}{\partial x^2} + \frac{\partial^2[\tilde{u}v^{\Phi} + \tilde{v}u^{\Phi}]}{\partial x\,\partial y} + \frac{\partial^2[\tilde{v}v^{\Phi}]}{\partial y^2}\right), \tag{11}$$

$$\frac{\partial^2 P_i^{\Phi}}{\partial x^2} + \frac{\partial^2 P_i^{\Phi}}{\partial y^2} = -\left(\frac{\partial^2\{u'^2\}^{\Phi}}{\partial x^2} + 2\,\frac{\partial^2\{u'v'\}^{\Phi}}{\partial x\,\partial y} + \frac{\partial^2\{v'^2\}^{\Phi}}{\partial y^2}\right), \tag{12}$$

where the above equations are solved with compatible boundary conditions. Note that the phase-averaged portions

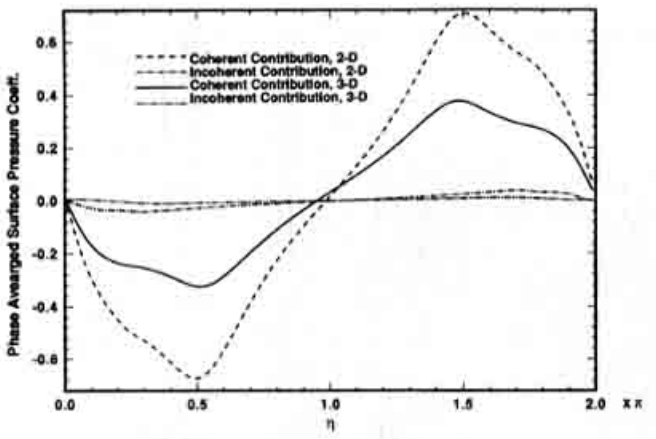

FIG. 22. Surface distribution of the coefficients of the coherent and incoherent components of the phase-averaged pressure obtained for Case II at a phase corresponding to the maximum lift. Results of both 2-D and 3-D simulations have been plotted for comparison.

of the Reynolds normal and shear stresses, $\{u'^2\}^{\mathcal{P}}$, $\{u'v'\}^{\mathcal{P}}$, and $\{v'^2\}^{\mathcal{P}}$, are, in general, nonzero due to their nonlinear nature. We present results for Case II in the subsequent discussion and it is found that the other cases exhibit similar overall behavior.

In Figs. 21(a) and 21(b) we have plotted contours of the coefficient of the phase-averaged part of pressure at the phase corresponding to maximum lift for the 2-D and 3-D simulations, respectively. In both these figures, it can be seen that the distributions are almost exactly antisymmetric, with a low-pressure region in the top half of the wake and a similar high-pressure region in the bottom half of the wake. This induces a low pressure on the top surface and a high pressure on the bottom surface of the cylinder, thereby producing a net positive lift. It should be noted that the above phase-averaged pressure field will produce very little net drag, due to the fact that the pressure field is almost antisymmetric about the $\eta=0$ symmetry line. Corresponding plots at the point of minimum lift are mirror images of Figs. 21(a) and 21(b) about the symmetry line.

In Fig. 22 the surface variation of the coherent and incoherent contributions of the phase-averaged pressure coefficient have been plotted for the 2-D and 3-D simulations at a phase corresponding to maximum lift. First, we observe that the contribution of the incoherent component is small and the phase-averaged pressure is determined mainly by the coherent component. As noted earlier, this is to be expected at the moderate Reynolds number considered in the present study. At higher Reynolds numbers, higher harmonics will be energized and will make a more significant contribution. In fact, the experiments of Cantwell and Coles[22] at a much higher Reynolds number of 140 000 show that the incoherent contributions to Reynolds stresses is higher than the contribution from the coherent phase-averaged motion, and therefore their effect on surface pressure variation may not be negligible at higher Reynolds numbers. Figure 22 also shows that the phase-averaged surface pressure is significantly higher in magnitude in the 2-D simulation, thus leading to a larger peak-to-valley lift fluctuation in the 2-D simulation.

The higher magnitude of phase-averaged surface pressure for the 2-D simulation shown in Fig. 22 can be traced back to the phase-averaged pressure distribution shown in Fig. 21. A comparison of the pressure coefficient distribution in Figs. 21(a) and 21(b) shows that even though the magnitude at the center of the intense phase-averaged pressure in the near wake is roughly the same for the two simulations, the center is itself located closer to the cylinder for the 2-D simulation. Physically, this implies that during the shedding cycle, the vortices approach closer to the base of the cylinder in the 2-D simulations and thereby lead to a larger amplitude of fluctuations in the lift force.

The antisymmetric nature of the phase-averaged pressure and its strong effect on lift, but not on drag, is in stark contrast to the distribution of mean pressure [Figs. 10(a) and 10(b)], which is symmetric about the $\eta=0$ and contributes mainly to the drag and nothing to the lift force. It is noted that the lift fluctuates at the fundamental shedding frequency, whereas the drag oscillates primarily at the first harmonic. This explains the observation that the phase-averaged pressure (which only contains the contribution from the fundamental frequency) is antisymmetric and does not make any contribution to the drag fluctuation. To study the fluctuations in drag, one needs to consider the pressure component that is phase averaged with respect to the first harmonic, which is computed as follows:

$$P_{\mathrm{II}}^{\mathcal{P}}(\xi,\eta)=\frac{1}{T}\frac{1}{L_z}\int_0^{L_z}\int_0^{T}P(\xi,\eta,z,t)e^{-i(4\pi/T)}\,dt\,dz. \tag{13}$$

Figure 23(a) shows this pressure coefficient for the 3-D simulation of the circular cylinder at a phase corresponding to the maximum drag. It can be readily observed that the pressure distribution is symmetric about the $\eta=0$ symmetry line, and thus this component will mainly affect the fluctuation in drag and will have very little effect on the fluctuation of lift. Furthermore, it is also observed that at this phase, a low-pressure region is situated at the base. The surface distribution of this pressure component at the phase corresponding to maximum drag is shown in Fig. 23(b), and it is observed that there is a narrow region of low pressure located in the base, whereas the rest of the cylinder experiences a slight high pressure. The peak in the drag is found to be mainly due to the low-pressure region at the base. The situation is reversed at the phase corresponding to the minimum drag, and the surface pressure distribution at this phase shown in Fig. 23(b) reveals a high-pressure region in the base of the cylinder.

IV. CONCLUSIONS

It is found that even in the absence of extrinsic three-dimensional effects, the lift and drag forces on elliptic and circular cylinders computed from 2-D simulations differ from those computed from 3-D simulations. Furthermore, the drag and base pressure coefficients computed from the current 3-D simulations matches well with experimental results, indicating that it is primarily intrinsic three-dimensional effects that lead to the discrepancy between experimentally measured lift and drag forces and those computed from 2-D simulations. An important finding of the present study is that

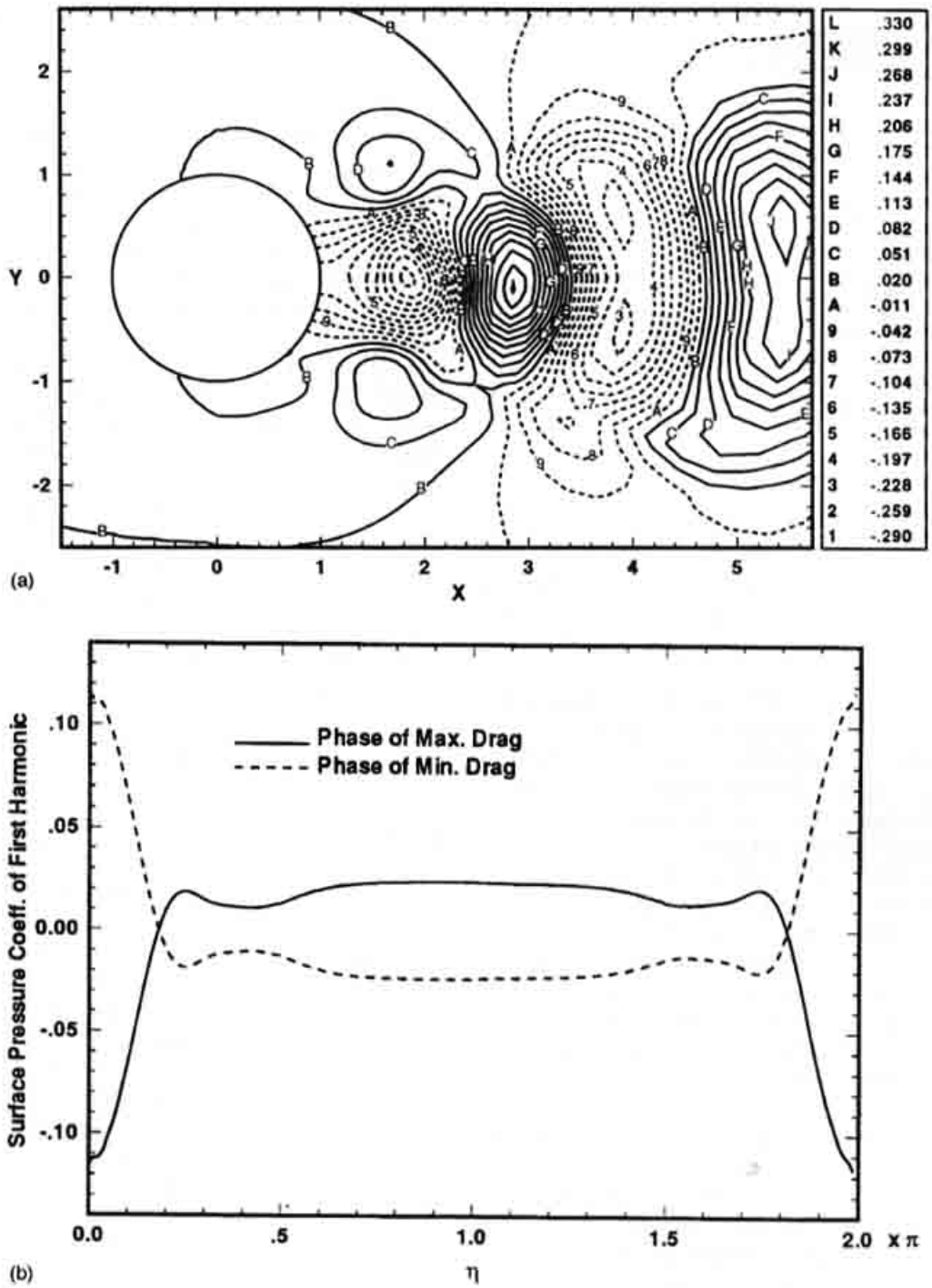

FIG. 23. (a) The coefficient of the first harmonic component of pressure [see Eq. (13)] obtained from 3-D simulation of Case II. Phase is chosen to correspond to the instant of maximum drag. Solid and dashed contour lines correspond to positive and negative values, respectively. (b) Surface distribution of the coefficient of the first harmonic component of pressure coefficient obtained from 3-D simulation of Case II at phases corresponding to maximum and minimum drag.

the difference between the drag computed from 2-D and 3-D simulations is very much dependent on the cylinder geometry, and is found to be more significant for bluffer bodies.

The direct effect of the mean flow field on the mean pressure is separated from that of the Reynolds stresses, and it is found that higher in-plane Reynolds stresses are the main cause for the overprediction of drag in 2-D simulations. Comparison of mean flow fields obtained from 2-D and 3-D simulations reveals that on average, the Kármán vortices roll up closer to the cylinder for 2-D simulations. However, this does not have any significant effect on the mean drag. The length of the wake does, however, have an indirect bearing on the surface pressure in that for the 2-D simulations, which exhibit a shorter wake, the region of intense Reynolds

stresses in the wake lies closer to the cylinder, thereby increasing the effect of the Reynolds stresses on the surface pressure.

Large secondary vortices are observed in the mean flow pattern obtained from the 2-D simulation of flow past the circular cylinder. In contrast, the secondary vortices formed in 3-D simulations are smaller and fewer in number. However, the presence of these vortices does not have any noticeable effect on the surface pressure distribution for either 2-D or 3-D simulations, and thus, in contrast to Tamura *et al.*,[6] we conclude that these vortices are not the cause for the discrepancy between the drag computed from 2-D and 3-D simulations.

The shedding is found to be well correlated across the span, and thus the drop in the peak-to-valley level of lift cannot be attributed to the loss of spanwise correlation. The drop in the peak-to-valley level of lift is found to be primarily due to the excursion of the Kármán vortices about their mean position in the wake. It is found that these vortices approach closer to the cylinder surface during the shedding cycle in 2-D simulations, thereby inducing a larger-pressure fluctuation on the surface, which results in a larger amplitude of lift fluctuation.

Finally, the detailed comparison of 2-D and 3-D simulations presented in this study not only illustrates the limitations of two-dimensional approximations in predicting lift and drag forces over nominally two-dimensional bodies, but goes beyond that by providing a detailed view of the effect of unsteadiness and three-dimensionality on the surface pressure distribution and the aerodynamic forces for bluff body wake flows. The flow fields obtained in the present 2-D simulations can be considered as true representatives of natural two-dimensional flows occurring at lower Reynolds numbers (for example, at $49<Re<180$ in the case of a circular cylinder). Support for this assertion comes from the fact that the base suction pressure and drag obtained from the 2-D simulation of the circular cylinder at $Re^*=525$ falls close to the extrapolation of the experimental results obtained in the two-dimensional range of $49<Re<180$. Thus, a comparison of results obtained from 2-D and 3-D simulations performed at identical Reynolds number eliminates the complicating Reynolds number effect, and highlights only the differences arising from three-dimensionality.

ACKNOWLEDGMENTS

These computations have been performed on the Cray-YMP at the National Center for Supercomputing Applications at the University of Illinois at Urbana—Champaign and on the C-90 at the Pittsburgh Supercomputing Center. This research has been partly supported by the Schlumberger Corporation.

[1]C. H. K. Williamson, "The natural and forced formation of spot-like 'vortex dislocations' in the transition of a wake," J. Fluid Mech. **243**, 393 (1992).

[2]C. H. K. Williamson and A. Roshko, "Measurements of base pressure in the wake of a cylinder at low Reynolds numbers," Z. Flugwiss. Weltraumforch. **14**, 38 (1990).

[3]C. H. K. Williamson, "Vortex dynamics in the cylinder wake," to appear in Annu. Rev. Fluid Mech.

[4]A. Roshko, "Perspectives on bluff body wakes," J. Wind Eng. Indus. Aerodyn. **49**, 79 (1993).

[5]K. Chua, D. Lisoski, A. Leonard, and A. Roshko, "A numerical and experimental investigation of separated flow past an oscillating flat plate," FED-Vol. 92, *International Symposium on Nonsteady Fluid Dynamics*, edited by J. A. Miller and D. P. Telionis, 1990, pp. 455–464.

[6]T. Tamura, I. Ohta, and K. Kuwahara, "On the reliability of two-dimensional simulation for unsteady flows around a cylinder type structure," J. Wind Eng. Indus. Aerodyn. **35**, 275 (1990).

[7]M. Hammache and M. Gharib, "A novel method to promote parallel and oblique vortex shedding in the wake of circular cylinders," Phys. Fluids A **1**, 1611 (1989).

[8]C. H. K. Williamson, "Oblique and parallel shedding in the wake of a circular cylinder at low Reynolds numbers," J. Fluid Mech. **206**, 579 (1989).

[9]V. V. Sychev, "Asymptotic theory of separated flows," Mekh. Zh. Gaza No. **2**, 20 (1982).

[10]R. Mittal and S. Balachandar, "Direct numerical simulation of flow past elliptic cylinders," submitted to J. Comput. Phys.; presently, TAM Report No. 751, UILU-ENG-94-6007, 1994.

[11]H. Mansy, P. Yang, and D. R. Williams, "Quantitative measurements of three-dimensional structures in the wake of a circular cylinder," J. Fluid Mech. **270**, 277 (1994).

[12]E. Meiburg and J. C. Lasheras, "Experimental and numerical investigation of the three-dimensional transition in plane wakes," J. Fluid. Mech. **190**, 1 (1988).

[13]F. M. Najjar, "Direct numerical simulations of separated and separated–reattaching flows on massively parallel processing computers," Ph.D. thesis, University of Illinois at Urbana—Champaign, 1994.

[14]R. Mittal and S. Balachandar, "Vortical structures in bluff body wakes," AIAA Paper 95-0867, 1995.

[15]R. Mittal and S. Balachandar, "Generation of streamwise vortical structures in bluff body wakes," submitted to Phys. Rev. Lett.

[16]R. Mittal, "Study of flow past elliptic and circular cylinders using direct numerical simulation," Ph.D. thesis, University of Illinois at Urbana—Champaign, 1995.

[17]C. Wieselsberger, "New data on the laws of fluid resistance," NACA Tech. Note TN 84, 1922.

[18]E. F. Relf, "Discussion of the results of measurements of the resistance of wires, with some additional tests on the resistance of wires of small diameter," British ACA R & M 102, 1914.

[19]A. Fage and F. C. Johansen, "The structure of vortex sheets," British Aerodyn. Res. Council R & M 1143, 1927.

[20]M. J. Lighthill, "Introduction. Boundary layer theory," *Laminar Boundary Layers*, edited by L. Rosenhead (Dover, New York, 1963), pp. 46–109.

[21]G. E. Karniadakis and G. S. Triantafyllou, "Three-dimensional dynamics and transition to turbulence in the wake of bluff objects," J. Fluid Mech. **238**, 1 (1992).

[22]B. Cantwell and D. Coles, "An experimental study of entrainment and transport in the turbulent near wake of a circular cylinder," J. Fluid Mech. **136**, 321 (1983).

[23]R. D. Henderson, "Unstructured spectral element methods: Parallel algorithms and simulations," Ph.D. thesis, Princeton University, 1994.

[24]S. Sakamoto, S. Murakami, and A. Mochida, "Numerical study of flow past 2D square cylinder by large eddy simulation: Comparison between 2D and 3D computations," J. Wind Eng. Indus. Aerodyn. **50**, 61 (1993).

[25]W. C. Reynolds and A. K. M. F. Hussain, "The mechanics of an organized wave in turbulent shear flow. Part 3. Theoretical models and comparisons with experiments," J. Fluid Mech. **54**, pp. 263–288 (1972).

[26]S. C. R. Dennis and G-Z. Chang, "Numerical solutions for steady flow past a circular cylinder at a Reynolds number up to 100," J. Fluid Mech. **42**, 471 (1970).

[27]C. Norberg and B. Sunden, "Turbulence and Reynolds numbers effects on the flow and fluid forces on a single cylinder," J. Fluids Struct. **1**, 337 (1987).